Study of Charge Carrier Dynamics in Methylammonium Lead Iodide with Electron and Hole Transport Layer under Bias Light

Kousumi Mukherjee

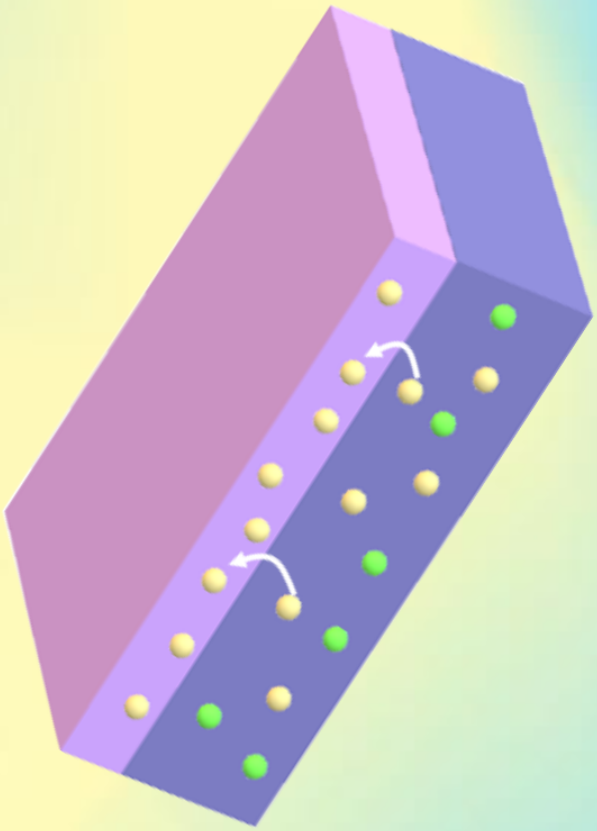

TU Delft

Study of Charge Carrier Dynamics in Methylammonium Lead Iodide with Electron and Hole Transport Layer under Bias Light

by

Kousumi Mukherjee

to obtain the degree of Master of Science
at the Delft University of Technology,
to be defended publicly on Thursday May27th, 2021 at 9:30 AM.

Student number:	5039789	
Project duration:	August, 2020 – April, 2021	
Daily Supervisor :	Valentina Caselli	
Thesis committee:	Dr. T J. Savenije,	TU Delft, supervisor
	Dr. F. Grozema,	TU Delft

TU Delft

Preface

This scientific report is written to finalize the thesis project. This project is part of the curriculum for obtaining a master's degree in Chemical Engineering. It was done under the supervision of Prof. Tom Savenije and Valentina Caselli. I would like to thank both of them for helping me out during the course of the thesis and also for their advises regarding my future career paths. Their guidance in every step had helped me in understanding this interesting topic better and had been most valuable. Special thanks to Jos Thieme, for helping me a lot with the laser setup and Nicky Dusoswa for all the instructions about the Dektak measurement and UV-Visible spectroscopy. I am also thankful to Jiashang Zhao for helping me in the lab whenever needed. Last but not least, I would like to thank all the Optoelectronic Materials group members and perovskite group members for your guidance during the discussions which had helped me shape my thesis eventually .

Kousumi Mukherjee
Delft, April, 2021

Abstract

Perovskite solar cells had been introduced in 2009 and had seen a huge increase in their efficiency since then. Here, the perovskite material absorbs photons and creates electron-hole pairs. These charges are then extracted by the electron transport layer and the hole transport layer to the respective electrodes. Here, a bi-layer system of the perovskite material and an/a electron/hole transport layer is considered. Methylammonium lead iodide, C_{60} and Spiro-MeOTAD are used as the perovskite material, ETM and HTM respectively.

There have been many studies to increase the PCE of perovskite solar cells. The PCE depends on the open circuit voltage (V_{OC}) which is still under the highest achievable limit. In this study, we have studied the charge carrier dynamics which affects the V_{OC}. We have studied the bi-layer system, mentioned above, under continuous illumination condition, by time resolved microwave conductivity (TRMC) and also in absence of it. Under illumination, in open circuit condition here, the generated charges move to their respective transport layer but they are not extracted out of the system. Subsequent saturation of the transport layer can take place at high photon fluence due to presence of the excess number of charge carriers present in it. This can affect the charge carrier dynamics across the interface. Continuous illumination can also affect the interface of MAPI and transport layer. This is also studied here.

It is seen that there is an efficient charge transfer to the C_{60} ETL and Spiro-MeOTAD HTL under pulsed laser excitation at 650nm from both TRMC and PL measurements. Under bias illumination, C_{60} gets saturated at high intensity of bias illumination. The number of traps in the system increases after illumination. The MAPI | Spiro-MeOTAD bilayer system gets degraded but this degradation can be prevented at low temperature. This was attributed to the quenching of ion mobility at low temperatures. Further, the curve fitting of the TRMC traces obtained were done to find the kinetic parameters.

Glossary

ETL Electron Transport Layer. v, 4, 6–8, 20, 22, 24, 25

ETM Electron Transport Material. v, 4, 7

FAPI Formamidium Lead Iodide. 2

HOMO Highest Occupied Molecular Orbital. 3, 6, 8, 9

HTL Hole Transport Layer. v, 3, 6–9, 20–22, 24, 31, 35

HTM Hole Transport Material. v, 3, 4, 6, 9, 31

LUMO Lowest Unoccupied Molecular Orbital. 4, 6, 8, 25

MAPI Methylammonium Lead Iodide. v, ix, 2, 4–8, 15, 19–33, 35, 41, 42, 45–47

PCE Power Conversion Efficiency. v, 3, 4, 6

PL Photoluminescence. v, 8, 20, 21, 35

TRMC Time Resolved Microwave Spectroscopy. v, ix, 4, 7, 13–15, 20, 22–26, 32, 35

XRD X- Ray Diffraction. 19, 41

Contents

1

Introduction

The switch to alternative energy sources has become an important subject in today's world with the ever increasing power demand and the decreasing reserve of the fossil fuels. Solar energy is one of the most promising and efficient source of renewable energy as it is available in abundance even though it is of intermittent nature. The photovoltaic technology has evolved from the silicon solar cell which was the first generation solar cell. They are efficient but their processing cost is quite high and the side products from its manufacturing are not environmental friendly. It was followed by solar cells using thin film of inorganic compounds like $CdTe_2$ and CIGS as the second generation and the organic solar cells and dye sensitized solar cells as the third generation. The latest (fourth) generation is the perovskite solar cell and its efficiency has reached to 25.5%.[1],[2] They are quite efficient due to their high carrier mobility, diffusion length, high absorption coefficient, low exciton binding energy, tunable and optimum band gap. Unfortunately, one of its main shortcomings is its instability.[3],[4]

In a perovskite solar cell, electron - hole pairs are generated when the perovskite material is photoexcited. Then, the holes are extracted to the anode while the electrons are extracted by the cathode. There are two main device architecture:

- Mesoporous structure - Perovskite material is formed on porous semiconductor metal oxide resulting in an interpenetrating network of the two. The electrons are extracted by this metal oxide and transported to the cathode whereas the holes move to the anode along the domain of the perovskite.[5]

- Planar structures - There are two interfaces with the perovskite material and the transport layer. A n-type electron transport layer is used to transport the electron to the cathode while a p-type hole transport layer extracts the hole to the anode from the perovskite. Depending on the side of illumination it can be either n-i-p or inverted p-i-n planar structure. [6]

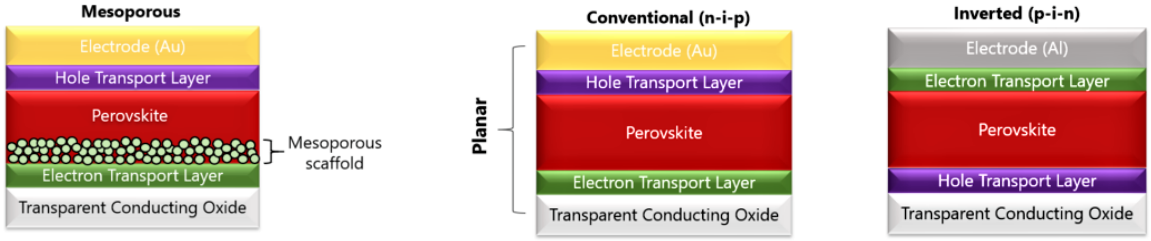

(a) Mesporous (b) Conventional planar structure (c) Inverted planar structure

Figure 1.1: Perovskite Solar Cell architecture [7].

The properties and types of various perovskite material and transport layers are going to be explained in the upcoming sections.

1.1. Perovskite Materials

Perovskites, in general, is a class of crystals with the formula ABX_3 where X is an anion, A is a cation in the cubo-octahedral site and B is a cation in the octahedral site. If X is a halide (chlorine (Cl^-), bromine (Br^-), iodine (I^-)), then B is a divalent cation like lead (Pb^{2+}), tin (Sn^{2+}), etc. while A is a monovalent cation. A can be an organic radical like methylammonium ion (MA : $CH_3NH_3^+$) and formamidinium ion (FA : $NH2CHNH_2^+$) or a metal ion like caesium (Cs^+), potassium (K^+), etc.[8]

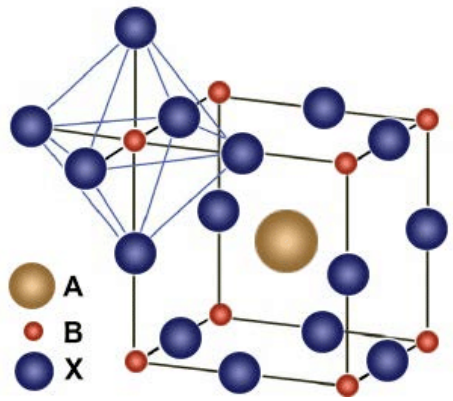

Figure 1.2: Perovskite structure [9]

An ideal perovskite crystal has a cubic structure possessing the highest symmetry. The Goldschmidt tolerance factor (t) can be used to find the tendency to form the perovskite structure.[10] It can be expressed as :

$$t = \frac{R_A + R_X}{\sqrt{2(R_B + R_X)}} \tag{1.1}$$

where, R_A, R_B and R_X are the ionic radii of A, B and X. For a stable structure, t should lie between 0.88 and 1.1. Another parameter used for defining the stability and the distortion of the perovskite structure is the octahedral factor (μ). The perovskite crystal is stable for μ ranging from 0.45 to 0.89. It can be expressed as:

$$\mu = \frac{R_B}{R_X} \tag{1.2}$$

Some of the commonly used perovskite materials are:

- Methylammonium Lead Iodide (MAPI)- It is one of the most commonly used perovskite material for use in perovskite solar cells due to its good opto-electronic properties.One of the disadvantage of this material is its short lifetime when it is exposed to humidity.
- Formamidium Lead Iodide (FAPI) - Here, the cation A is the formamidium ion with a larger radius than the methylammonium ion resulting in an increase in the tolerance factor. It has a band gap of nearly 1.47eV and a better optical absorption than MAPI. The main advantage of FAPI over MAPI is that it doesn't undergo structural phase transition within the operating temperature range.[11]
- Mixed Halide perovskite- This type of perovskite contain two types of halide ions in it, for instance $CH_3NH_3PbX_xY_{3-x}$ (X,Y = Br, Cl, I).They have tunable band gaps by changing the stoichiometric ratio of the halide ions. This changes the optical absorption band. They have better carrier transport than its pure iodide equivalent. [12]

- Lead Free Perovskite- Due to the toxic nature of lead and its solubility in water, there is an increase in the study of lead free perovskites. One of the replacement is the tin based perovskite but they are at a disadvantage due to their instability and low performance. Another type is the double metal halide perovskites of the formula $A_2BB'X_6$, where A is a monovalent cation, and B and B' are a monovalent cation (eg. Na^+, Ag^+, Rb^+) and trivalent cation (eg. Bi^{3+}, Sb^{3+}) respectively acting as the replacement of lead. Their synthesis is difficult due to the formation of undesired phases.[13]

Perovskite films can be deposited by a variety of low temperature processes.[11] Some of them are:

- Spin coating - It can be a single step deposition where the precursors mixed in an aprotic polar solvent is first spin coated on the substrate. The solvents have a low vapour pressure and high boiling point at room temperature. A crystallised layer of perovskite is formed due to self assembly and evaporation of solvent occurred during spinning and annealing. It can also be a two step sequential deposition process where one of the precursor is first deposited followed by the spin coating/ dip coating of the other. Parameters such as spinning speed, spinning time, dipping time, dipping concentrations, etc affect the film properties.

- Rapid deposition crystallisation - Here, an antisolvent, such as benzene, xylene, etc., is dripped over a perovskite layer to increase the nucleation of the film and the growth rate of the crystals.

- Thermal evaporation- The precursors salts are evaporated and deposited simultaneously from two sources or sequentially in a nitrogeneous environment. This process helps in making films with uniform crystalline platelets.

- For large scale production, drop casting, inkjet printing, coating with doctor blade, atmospheric layer deposition (ALD) [14] can be used.

1.2. Transport Layers

Hole Transport Layer

These materials act as hole selective material with good hole mobility, a HOMO level close to the valence band edge of the perovskite material and good UV and thermal stability. They enhance the hole collection and reduces charge recombination. They are less conductive than the perovskite materials and this increases the series resistance and also decreases the Fill Factor of the cell. So, highly conductive Hole Transport Material (HTM) increases the Fill Factor of the solar cells. HTM can be - conducting polymers like polythiophene based conducting polymers (eg. P3HT), organometallic compounds (eg. copper pthalocyanine), metal oxides (eg. nickel oxide, molybdenum oxide) and small hole conducting molecules (eg. Spiro-MeOTAD). Some of the HTM are described below:

- Spiro-MeOTAD - It is an organic molecule which can be easily deposited on the perovskite as it is solution processible. This material has a low hole mobility affecting the conductivity of the material which is a main disadvantage of this material. In order to increase the conductivity of this material, additives can be added as dopants but they may lead to device instability. Some of the dopants are lithium and antimony based salts, cobalt (III) based salts, organic compounds like F4-TCNQ, TBP, etc. [15] The Ionization Energy is in the range of -6.3eV to -4.7eV depending on the dopants and its concentration used, environmental condition during preparation, chemical interaction with the layer on which it is deposited, etc.[16]

- Nickel Oxide (NiO_x)- It is a cubic p-type semiconductor with nickel in its +3 or +4 oxidation state. It has a wide energy band gap of 3.5-4eV. A high PCE can be obtained as compared to other inorganic HTM due to its deep work function of -5.3eV and high transmittance.

- Poly(3-hexylthiophene-2,5-diyl) (P3HT)- Thiophene is a heterocyclic compound to construct the conjugated polymer donor. It has a higher hole mobility than Spiro-MeOTAD, excellent solubility and good crystallinity due to the well defined molecular structure.[11]

- Copper iodide (CuI) - It is a highly conductive p-type conductor with a wide band gap of 3.1eV and a work function of -5.1eV. It is cheap, chemically stable and solution processible. [17]

Electron Transport Layer

An Electron Transport Material has its LUMO energy level lower than the perovskite material's conduction band for transfer of electrons and a high transmittance in the visible range so most of the incident photons are absorbed by the perovskite material. It should also have a good thermal stability, resists degradation and non toxicity.
Some of the ETL which are commonly used are :

- Buckminister Fullerene (C_{60})- Ultrathin C_{60} layer has shown to effect the performance of perovskite solar cells positively.
- Titanium Oxide (TiO_2) - It is a large band gap semiconductor of band gap 3.2eV and 3.02eV for anatase and rutile phase respectively. It blocks holes efficiently due to low valence band level. It has high electron mobility, good optical transparency, easy preparation, long electron lifetime and good environmental stability. However, its main disadvantage is the poor conductivity of its film.[18]
- Zinc Oxide (ZnO) - It is a low cost material with high electron mobility and wide band gap of 3.3eV with large exciton binding energy of 60meV. Its conduction band minimum is at 4.2eV. It can be synthesised easily. Its high ionization potential helps in blocking holes in moving into the ETL from the perovskite.[19]

1.3. Scope and Outline of Project

MAPI has already been used to produce perovskite solar cell and also in tandem structure with silicon.[20] There have been many research to increase the efficiency of the solar cells. Here, a study is made on the charge carrier dynamics which severely affects the efficiency of the solar cells. Firstly the charge carriers dynamics in perovskite absorber material is studied followed by its transfer to the transport layers by TRMC.

In order to increase the PCE of the solar cell, the open circuit voltage should be increased which in turn is affected by the kinetics of the charge carriers. So, next a study of the charge carrier dynamics under illumination is done. Under illumination in open circuit condition, fermi level splitting takes place resulting in creation of an open circuit voltage. Charges generated move to their respective transport layer and subsequent saturation of the transport layer can take place which may affect the charge carrier dynamics across the interface of perovskite and transport layers. Saturation of the transport layer will prevent any extra charge carriers from being extracted by the transport layer due to the absence of the electric field to drive the extraction. The resulting charge carrier dynamics in perovskite - transport layer bi-layer system should then reflect that of the monolayer perovskite. Changes in the kinetic parameters like increase in the interfacial recombination shows that the interface is affected. So, this study will help us understand whether the interface of the perovskite transport layer will be affected or not under bias illumination and thus will help know further how it can be improved.

In Chapter 2, a literature review along with some theory is present on the properties of the perovskite material, ETM and HTM being used. It is followed by the study of charge carrier dynamics which had already been studied before. Then the effect of illumination on perovskites has been studied. In Chapter 3, the preparation of the bilayers are discussed followed by the characterization techniques which are used in this study. In Chapter 4, the results that we have got from the experiments conducted are presented and discussed. It is followed by the conclusions which can be drawn from the results and some recommendations for further work in Chapter 5.

2

Literature Review

In this study, MAPI is chosen as the perovskite material. It has high optical absorption coefficient, favourable band gap, long carrier diffusion length (of more than 100nm [21]) and good electrical transport properties. The tolerance factor calculated for this material is found to be 0.83 using the methylammonium cation radius as 1.8Å, making it a stable structure.[8] There is a change in the structure from cubic to tetragonal at around 300K which is in the working temperature range of the solar cell due to a partial separation of the lead iodide from the perovskite phase.[22] The valence band maximum and the conduction band minimum are estimated to be -5.43eV and -3.93eV respectively resulting in a band gap of 1.5eV.[23] The onset of absorption is calculated to be 826nm from this. As it has a high optical absorption coefficient, wavelength of light at 700nm and 550 nm can be absorbed by a thin layer of this material of thickness 0.66μm and 2μm respectively.[8] So, most of the incoming light can be absorbed by this material in the solar cell as only a thin layer is used. The excitons formed is weakly bound (binding energy is comparable to thermal energy at room temperature) and free charge carriers are produced resulting in high open circuit voltage.

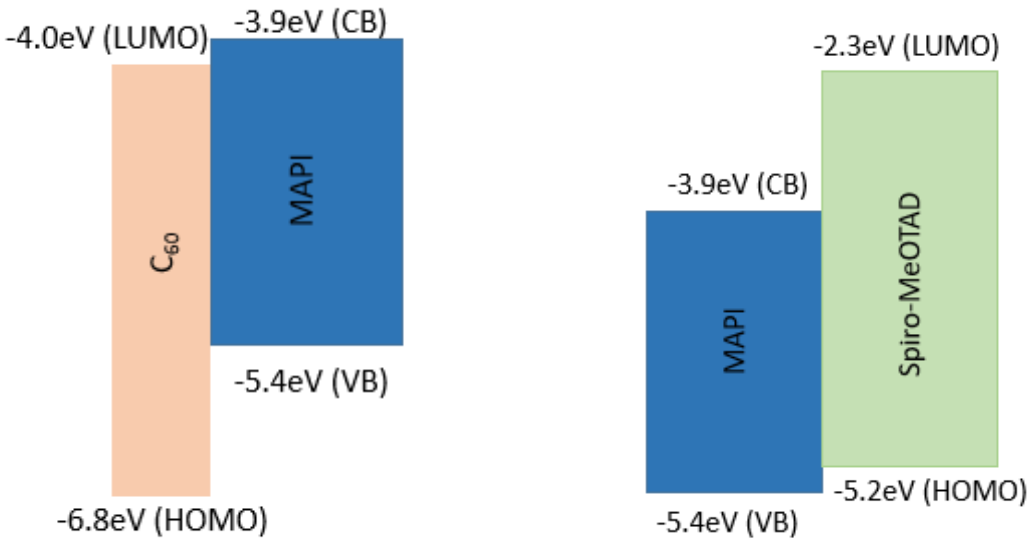

(a) Band diagram of MAPI | C[24]

(b) Band diagram of MAPI | Spiro-MeOTAD [25]

Figure 2.1: Band diagram of MAPI and transport layer in dark

Spiro-MeOTAD is used as the HTL. The advantage of using this material as a HTM is its well matched energy levels with MAPI, minimum absorption in the visible and near infrared range of solar spectrum, high melting temperature and solution processibility. The offset between its HOMO level and valence band of MAPI is around 0.2eV.[26] So, the HOMO is close to the Fermi energy level.

C_{60}, is chosen as the ETL due to good alignment of its energy level with that of MAPI. It has a HOMO level at nearly -6.8eV and LUMO level nearly at -4.0eV. [24] A 20nm C_{60} layer shown to exhibit a charge carrier mobility of about $1.6*10^{-4}m^2V^{-1}s^{-1}$. The offset is nearly 0.1eV and remains constant with C_{60} thickness. It can extract electrons efficiently from the perovskite and has a high injection barrier for holes. It is proposed that there is a possible passivation of the traps at the MAPI surface by C_{60}. An efficient electron transfer is seen. So, the C_{60} has a high electron density and a low hole density, [27]

On photoexcitation, free charge carriers are produced. The electrons are excited to the conduction band and holes are created in the valence band. The electrons move to the C_{60} layer while the hole moves to the Spiro-MeOTAD. Proper alignment between the energy level of the MAPI and the ETL and HTL results in efficient charge injection into the transport layer and reduces the charge recombination. The conductivity or mobility of the charge carriers in the transport layer also affects the performance. The alignment of the conduction band with LUMO level of an ETL creates an electric field for the electrons to move into the transport layer by drift. A similar electric field is created by the valence band of the perovskite and the HOMO level of the HTL for the holes to get injected in it. Low mobility results in high series resistance which causes accumulation of charges in the interface of perovskite and ETL (or HTL) . This can cause significant recombination with holes (or electrons) in the perovskite layer. [28]

The free charge carriers may also get trapped in a defect (also can be referred to as 'traps'). Traps can have an interband energy level or be present above the conduction band or below the valence band. In the latter cases, it can be considered not to harm the system. Depending on the nature of the trap in the former case, it may escape back to its excited energy level by absorbing thermal energy or by optical excitation, or it may recombine back. Traps result in a decrease in the PCE and open circuit voltage (V_{OC}).

Traps can be of 2 types- shallow traps and deep traps as shown in 2.2. Shallow traps exist near the conduction band or valence band edge such that the energy gap i.e. the difference in energy of the trap and the conduction/ valence band, is less ($E_G \leq k_BT$). Charge carriers trapped here are excited back thermally at non temperature. So, the charge carriers again contribute to the free charge carrier and hence only their mobility is hindered. Deep traps are present towards the middle of the band gap ($E_G \geq k_BT$) and it forms a pathway for non radiative recombination. MAPI can have intrinsic defects and surface defects caused by vacancies of methylammonium ion, lead and iodine, interstitial presence of methylammonium ion, lead and iodine and substitutions. [29]

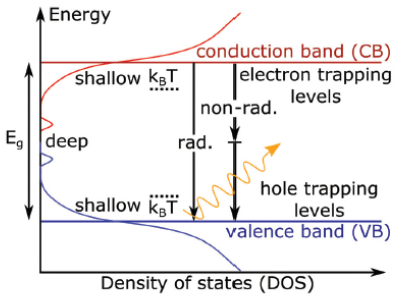

Figure 2.2: Electronic structure of traps [29]

Charge trapping becomes an important factor as it decreases the lifetime of the charges. Recombination of the trapped charge dominates over charge injection in the transport layer if trapping rate is higher. Several defect curing and surface passivation techniques have been studied in order to increase the open circuit voltage and PCE. An ultrathin interlayer of Poly (methyl methacrylate) (PMMA) has been seen to reduce the interface recombination and passivate the trap states.[30] Some other materials to show surface passivation effect are Organic halide salt- phenethylammonium iodide (PEAI) [31] and another Lewis base - poly-vinylpyrrolidone (PVP). The latter had been seen to show surface passivation effect by stabilization of the structure [32] and passivating Pb^{2+} defect.[33] Addition of a ultrathin polystyrene (PS) layer has also shown to increase the PCE.[34] The thin layer is seen to pas-

sivate the traps and defects in the interface of Spiro-MeOTAD HTL and perovskite material and also its hydrophobic nature prevents moisture infiltration.[35] It also acts as an insulating tunneling junction and suppresses interface recombination by allowing only one type of charge to pass through.[36] When used as a blend with PCBM it also improves the ETM film uniformity along with decreasing recombination of electrons and holes in ETL.[37]

2.1. Study of charge carrier dynamics in MAPI and Transport Layers with TRMC

Study of charge carrier dynamics in the photo-active materials and the transport layer is important in order to know the properties of charge carriers related to charge injection and recombination. When the photo-active material (here, MAPI) is excited by a pulsed laser, free electrons and holes are generated. Initially, charge transport within the perovskite layer and charge injection in the transport layers takes place. The photoexcited electrons may also recombine back with the holes in the MAPI. Due to the absence of electrodes, charge extraction is not possible and charges will start accumulating in the transport layers. These charges can recombine via the interface of the MAPI - transport layer ('interfacial recombination'). While considering the MAPI - C_{60} system, the transfer current density for electrons can be calculated as :

$$J_{T,n} = qS_T(n_{b,int} - n_{q,int}\exp -\frac{\Delta W_C}{k_B T}) \tag{2.1}$$

where, q is the elemental charge, S_T is the transfer velocity, $n_{b,int}$ and $n_{q,int}$ are the electron density at the interface of the perovskite and transport layer respectively, ΔW_C and $k_B T$ is the conduction band offset and the thermal energy respectively.[38] The accumulated electrons in the ETL attract the holes from the bulk through Coulomb interactions resulting in their build up at the bulk. The accumulated electrons slow down the transfer of electrons also. These factors results in increased interfacial recombination.[38]

TRMC measurement of MAPI had shown that with increased intensity of the pulsed laser i.e. at high photon fluence, band to band recombination became dominant over trapping of electrons. The charge carrier mobility was independent of the laser intensity. It was also found out that the number of photo-generated electrons is smaller than the concentration of the holes which could be due to background doping and/or photo doping. When a MAPI - Spiro-MeOTAD bilayer system was photoexcited, the total concentration of holes did not change appreciably suggesting that MAPI is unintenionally p-doped.
An efficient charge transfer has been observed in both the MAPI - C_{60} and MAPI - Spiro-MeOTAD bilayer system with an increase in lifetime of the charge carriers.[39] MAPI when photo-excited below the band gap, MAPI has shown charge carrier dynamics similar to above band gap excitation due to the presence of energy levels close to the valence band maxima and the conduction band minima followed by defect related absorption taking place at even lower excitation energy.[40]

2.2. Effect of illumination

At thermal equilibrium, the position of the Fermi level of as semiconductor depends on whether it is p-doped or n-doped. For instance, if it is p-doped then the Fermi level will be closer to the valence band and lower than the Fermi level of an intrinsic semiconductor E_{Fi}. On illumination, excess charge carriers are created and it is not in thermal equilibrium. Fermi level splitting takes place with a quasi-Fermi level for electron (E_{Fn}) and a quasi-Fermi level for holes (E_{Fp}).[41],[42] The position of these quasi-Fermi level can be defined as :

$$E_{Fn} = E_{Fi} + k_B T ln(\frac{n_0 + \delta n}{n_i}) \tag{2.2}$$

$$E_{Fp} = E_{Fi} - k_B T ln(\frac{p_0 + \delta p}{n_i}) \tag{2.3}$$

where, $\delta p = \delta n$ and is the excess carrier concentration, and n_0 and p_0 are the concentration of electrons and holes in equilibrium respectively.

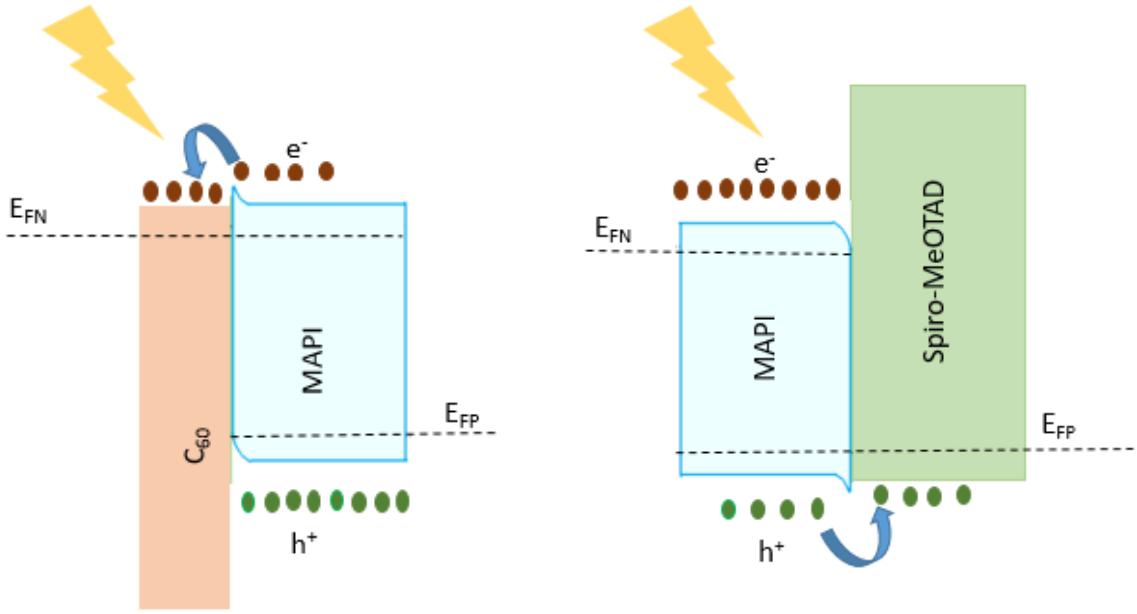

(a) Band diagram of MAPI | C_{60} under illumination

(b) Band diagram of MAPI | Spiro-MeOTAD under illumination

Figure 2.3: Band diagram under illumination showing Fermi level splitting and electron and hole transfer to the transport layers

In the perovskite - transport layer bilayer system, similar to other semiconductor materials, a built in potential exists in the dark. On illumination, Fermi level splitting takes place reduces the built in potential and a flat -band situation is approached. The dominant p-n junction of a perovskite solar cell is seen to form at the HTL or ETL interface depending on the ETL being used. [43] Band bending depends on the energy difference of the HOMO /LUMO level of transport layer and the perovskite material. Charges accumulation at this junction takes place due to higher band bending and device degradation is mainly initiated here. For instance, electrons accumulates near the HTL when dominant p-n junction is near the HTL. [44] The photoconductivity of the MAPI film has shown a weak change above the band gap but depends on the photon energy below it. It is found to be same before and after it has been illuminated for a time period of 1 hour in vacuum for photon energy greater than 1.6eV i.e. in the region of interband absorption. Below this energy level, there is an increase in the photoconductivity due to filling up or creation of interband states. [45]

On light soaking, MAPI films have show effect of both photo brightening and photodegradation by PL spectroscopy.[46] It was found out that this behaviour depends on the excitation wavelength. There is a transition between photodegradation and photo-brightening effect at nearly 520nm corresponding to the band gap of the residual PbI_2. Decomposition of MAPI takes place above PbI_2 band gap and possible photolysis of PbI_2, as shown in Equation 2.4 resulting in formation of I_2 triggers decomposition of MAPI. [47]

$$PbI_2 \overset{hv}{\rightleftharpoons} Pb^0 + I_2 \tag{2.4}$$

Due to energy alignment of valence band of MAPI and PbI_2, there is an efficient transfer of

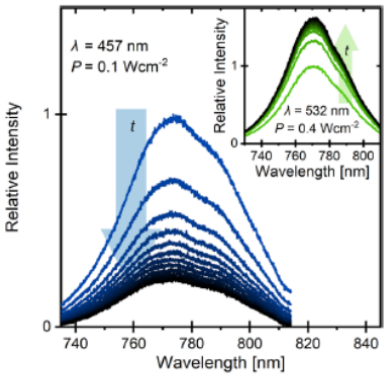

Figure 2.4: Photodegradation and photobrightening on illumination by different wavelengths of light.[46]

holes photoexcited from PbI_2 to MAPI valence band. These holes react with the iodine ions of MAPI to form PbI_2 as shown in Equation 2.5.This induces the degradation of the film.

$$2\,{I_{MAPI}}^{-1} + 2\,h^{+} \longrightarrow I_2 \tag{2.5}$$

It was also proposed that when high energy photons are used for illumination, excess phonons are created into the lattice due to the thermalization of the excited charge carriers. These phonons also provoke ionic defects once the illumination is removed.[48] Migration of mobile ions have also been found out. They are mainly intrinsic ions like iodine interstitial and vacancies due to their low activation energy and high mobility. These mobile ions accumulate at the perovskite transport layer interface due to the built in voltage of the perovskite solar cell. For instance, positive ions (eg. iodine vacancies) accumulate near the HTL as the electric field pushes the negative ions away from the HTM. These ions creates a Debye screening of the electric field in the perovskite bulk and reduces the efficiency of the charge extraction of the HTL. The inversion of the electric field due to the accumulated charges causes the electrons to flow towards HTL increasing the interface recombination. With prolonged illumination, negative ions starts accumulating at the HTL perovskite interface and acts as traps.[49]
Diffusion of iodine ions (I^-) in Spiro-MeOTAD HTL reduces the conductivity of the HTM. Iodine released from perovskite can also react with this ion resulting in the formation of triiodine ions (I^{3-}). These deepens the HOMO level of the Spiro-MeOTAD thereby forming an energy barrier for hole extraction. This decreases the hole extraction efficiency of the HTM.[50]
However, it has also been found out that under illumination, a large number of photo-excited charges are created. Some of them gets trapped in the vacancies created.The trap filling has shown to effect the system and create electric fields inducing the iodine vertical or lateral migration from the illuminated region to the dark region and changing the band bending on illumination. This migration of iodide ions may fill some of the vacancies resulting in a net decrease in the reduction in the density of vacancies.[51]
Light soaking has also shown effects of defect curing i.e. shallow traps being annihilated at room temperature by the excess carriers.[52],[53] These effects have been seen when wavelength of light is greater than 520nm.[46]

3

Experimental Methods, Characterization Techniques and Modelling of Charge Kinetics

3.1. Synthesis Methods

3.1.1. Preparation of Methylammonium Lead Iodide Perovskite Films

Lead acetate (obtained from Sigma Aldrich) and Methylammonium Iodide (synthesized in lab using standard procedure [23]) were used in 1:3 molar ratio and added in Dimethylformamide (DMF) to prepare the MAPI solution. It was mechanically stirred for 1 hour and then filtered. 120μL of the freshly prepared solution was spincoated on a plasma cleaned Quartz plate for 45s at 2000 rpm. Then, the samples were kept at room temperature for 15 minutes followed by annealing at 100°C for 5 minutes.

3.1.2. Deposition of C60 on MAPI film

C60 was deposited on the MAPI films with the help of an evaporator as shown in Figure 3.1.

A 30nm thickness film was obtained with the deposition rate of 0.3Å/s.

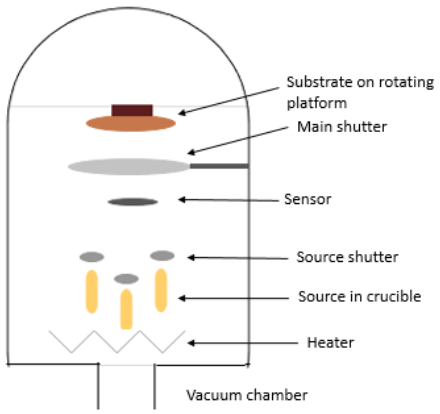

Figure 3.1: Thin film deposition by evaporation

3.1.3. Deposition of Spiro-MeOTAD film on MAPI film

A 75mg/mL of Spiro-MeOTAD solution was prepared in Chlorobenzene and mechanically stirred for 1 hour. 60μL of the filtered solution was spincoated on the MAPI films at 1500 rpm for 45s. They were kept at room temperature for 30 minutes followed by keeping it at 60° for 1 hour. The samples were kept overnight before any measurements were done.

3.2. Characterization of Samples

3.2.1. UV-Visible Absorption Spectroscopy

When light falls on a certain substance, it can be absorbed, transmitted or reflected by it. These interaction depends on the chemical and physical properties of the material and the energy and intensity of the light source used. UV- Visible spectroscopy involves the absorption, transmittance and reflectance of the material in the ultraviolet and visible region of the spectrum by means of transition of electrons within the molecules of the substance from a lower electronic energy level to a higher one by absorption.

The amount of absorption (A) or transmittance (T) by a sample can be found out with the help of the Beer - Lambert law which states that the absorbance of a substance is directly proportional to the path length (L) and molar attenuation coefficient or absorptivity of the species. The absorption and transmittance can be expressed as :

$$A = \mu L = -log_{10}T = -log_{10}(\frac{I}{I_O}) \tag{3.1}$$

where, μ is the attenuation coefficient, I and I_O are the intensity of the transmitted/ reflected light (depending on position of the sample) and incident light respectively.

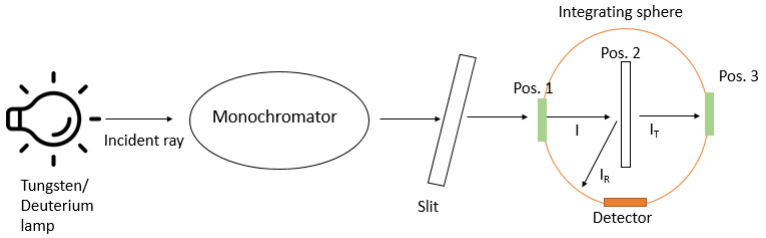

Figure 3.2: Set up of UV -Visible absorption measurement

Here, a spectrophotometer with a deuterium and tungsten halogen lamp is used to generate a stable light source spanning from UV- infrared region. The radiation is first split into specific wavelengths by monochromator. Then it passes through the sample. Depending on the position of the sample with respect to the integrating sphere as shown in Figure 3.2, the photodiode can measure the amount of transmitted and reflected light. The integrating sphere spatially integrates the diffuse reflectance and the transmitted light scattered from the sample measurements. If the sample is kept in front of the integrating sphere (Pos. 1), only the transmittance is measured whereas when it is kept at the end of it (Pos. 3), the amount of reflected light is measured. In order to get both the reflected and transmitted part , it needs to be kept inside the integrating sphere (Pos. 2).

Here, an UV- Visible absorption spectroscopy is done to know about the region (wavelengths) in which the perovskite and the transport layer mainly absorbs. A PerkinElmer LAMBDA 1050 spectrophotometer is used. The sample is placed inside the integrating sphere and the sum of $\%T$ and $\%R$ consisting of both the transmitted and reflective part respectively is measured from 250-850nm.

The fraction of photons absorbed by the sample can be found out by

$$F_A = 1 - (F_T + F_R) \tag{3.2}$$

After the baseline correction, the $\%T$ of a pristine quartz plate is measured so that the fraction of light absorbed by the quartz can be subtracted from the fraction of light absorbed by the thin film on quartz.

3.2.2. X-Ray Diffraction

X-ray diffraction is done to understand the crystalline nature of a material. A beam of x-ray is used as its wavelength is comparable to the interatomic distances. It is incident on the material to be studied, the X-ray gets diffracted by the (periodic) electron density of the atoms. Diffraction patterns are formed based on constructive and destructive interference of the diffracted beams. They add constructively in certain directions and it can be expressed by Bragg's Law as

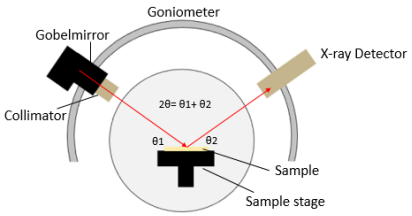

Figure 3.3: Schematic of θ- θ XRD set up

$$2d \sin\theta = n\lambda \tag{3.3}$$

where, θ is the incident angle of the X-ray, d is the distance between the diffracting planes, λ is the wavelength of the beam and n is any integer.
From a XRD measurement we can get the following data:

- The intensity tells about the unit cell content, crystal size, space group and symmetry.
- The position tells about the set of the crystal planes generating the diffraction pattern and the unit cell parameters (lengths and angles of the unit cell). It also depends on the wavelength of the X-ray source.
- The peak shape tells about the crystallinity , disorder and defects.

X-ray diffraction is used here to check the presence of the perovskite crystal and any impurities (for instance, lead iodide), if present. The quartz plate with the thin films of the perovskite and the transport layers, were mounted on a fixed plate. A theta - theta ($\theta - \theta$) geometry was used were the goniometer tube with X-ray source and detector rotates at θ°/min. A Bruker D8 Advance machine is used for measuring the X-ray diffraction by the samples made.Cobalt $k\alpha$ beam of wavelength λ = 1.789 °A is used by the machine. A scan from 2θ angle of 5-50° is used for measuring the XRD of MAPI, MAPI with C60 on top and MAPI with Spiro-MeOTAD on it.

3.2.3. Profilometry

A Dektak Profilometer is used to measure the film thickness. This instrument is used to measure the vertical profile, film thickness and topographical features of films. A diamond stylus of tip radius 12.5μm is put in contact with the sample and then moved laterally across it for a specified distance and time with a certain contact force. A part of the sample was scrapped off with solvent and it was measured in Hills and Valleys mode. The film thickness measured over atleast 5 places were averaged.

3.2.4. Time Resolved Microwave Spectroscopy

Time Resolved Microwave Spectroscopy (TRMC) is used for studying the charge carrier dynamics in the perovskite material. The semiconductor perovskite material is first excited with a pulsed laser beam resulting in generation of charges, and then a microwave is incident on it. The microwave is absorbed by the photo induced charged carriers thereby decreasing the microwave power. The decrease in microwave power is measured by a detector as a function of time. As the electric field of the microwave (in the GHz regime) interacts with the charge carriers resulting in the decrease of the power, this decrease in power is proportional to the change in conductance when the material is excited, which is given by

$$\frac{\Delta P(t)}{P} = -K\Delta G(t) \tag{3.4}$$

where, K is the sensitivity factor and ΔG is the change in photo-conductance. The change in conductance can be calculated by integrating the electrical conductivity (σ) of the sample over the complete

film thickness. The electrical conductivity of the sample depends on the product of the concentration of charge carriers and their mobility in the material. Hence, ΔG can be expressed as

$$\Delta G \propto \sigma = e(n_e\mu_e + n_h\mu_h) \tag{3.5}$$

where, e is the elementary charge, n_e and n_h are the concentration of the electrons and holes respectively, μ_e and μ_h are the mobility of electrons and holes respectively in the medium.[54]

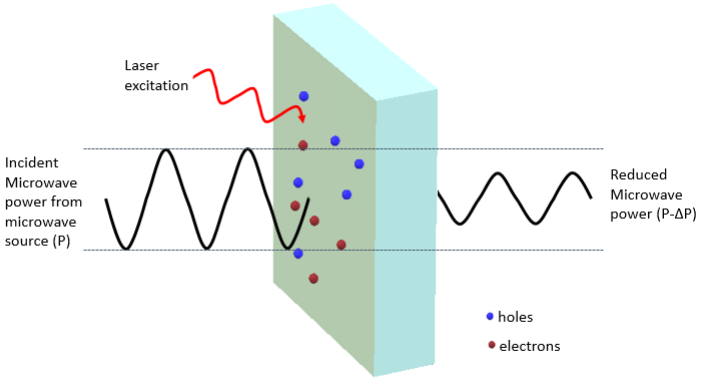

Figure 3.4: Schematic of creation of charges by laser pulse excitation and power attenuation of the microwave by the free charges used for the TRMC measurement

This method does not need electrodes. So, one of the advantages of studying the charge carrier properties by this method is avoiding any undesired chemical reactions and the interfacial effects between the electrodes and the perovskite or the transport layers. Another advantage is that we can study about both radiative and non radiative recombination via the trap states unlike in other methods like photoluminescence spectroscopy where the signal is produced from the radiative recombination. So, this method is quite useful for studying the perovskite and especially the interface of perovskite - transport layer pairs where the charges undergo both radiative recombination and nonradiative recominations by traps present on the surface, interface and the bulk.

In the TRMC set up being used for the experiment, a 10Hz pulsed laser is used. The beam passes through metallic neutral density filters with different optical density which are used to vary the number of photons incident on the sample. The study is conducted at a range of photon fluence by the help of these filters. The sample is placed in a gold plated microwave cell which transmits the laser pulse and reflects the microwave. Monochromatic microwaves (8.2 - 12.4 GHz frequency) generated by a voltage controlled oscillator is incident on the sample and a microwave circulator separates the reflected microwave of decreased power from the incident wave. This sample holder can be either an open cell or a cavity. The cavity has the cell partially closed by an iris. This is used to increase the sensitivity as compared to a measurement in the open cell by creating a standing microwave which leads to increased interaction with the sample. However, the response time of the open cell is less than that of the cavity. So, a very fast initial decay is not captured by a cavity as shown in Figure A.7. A diode detector converts it into a DC signal and to understand the change in photoconductivity due to the laser from the ΔP , an offset regulator is used to subtract the DC part to get the AC part. An amplifier is then used to amplify the signal. [54]

The output which is mainly obtained from the TRMC measurement is a trace of the normalised photoconductivity over a range of time. Initially there is an increase in signal as charge carriers are generated when the laser is incident on the sample followed by a decay which is due to the radiative and non radiative recombination taking place. A frequency scan of the sample placed inside the cavity gives the resonance frequency of microwave with respect to the sample and also tells about the conductivity of the sample when it is not excited by the laser.

The TRMC measurement of MAPI, MAPI with electron transport layer (C_{60}) and MAPI with hole transport layer (Spiro-MeOTAD) was done. The samples were excited at 650nm above the band gap of MAPI. The samples were excited from the side of the quartz (referred as 'backside') and also from the side of the films (referred as 'frontside').
For TRMC measurement of the samples in the presence of bias light was done with white light LED as the light source as shown in Figure 3.5. A convex lens and a semi transparent mirror were used to concentrate the incidence beam and to direct it on the sample as normal irradiance. A silicon photodetector with 7.9 mm diameter active area was used for the power measurement at the sample position.

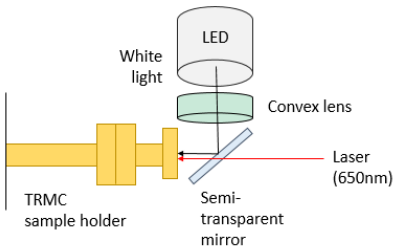

Figure 3.5: Schematic of experiment with TRMC in presence of Bias Light

3.2.5. Photoluminescence Spectroscopy

Photoluminescence is used for analysis of semiconductors and is a non-contact and non-destructive method. It is emission of light by a substance around band gap wavelength when it is irradiated by light with photon energy above the band gap of the material. The photoluminescence (PL) efficiency (η) is the ratio between radiative photolumienscence (I_{PL}), due to band to band recombination of electron and hole, to nonradiative recombination (I_{NON}) due to Auger recombination or defect trapping. It is expressed as :

$$\eta = \frac{I_{PL}}{I_{PL} + I_{NON}} \tag{3.6}$$

In steady state photoluminescence experiment, the samples- MAPI and MAPI with transport layers, are excited with a red laser (635nm) which is above the band gap of MAPI. A 665nm red light filter was used to filter out the red laser light from the detector. The photons emitted due to band to band recombination were then measured by the detector. An average of 100 and an integration of 70 were used to get a proper plot.

3.3. Modelling of Charge Kinetics

3.3.1. Modelling of Kinetics of Charges in MAPI

When a semiconductor material is excited above its band gap, electrons are excited to a higher electronic level in the conduction band leaving behind the holes in the valence band. Depending on the exciton binding energy of the material, these charges can either be free and mobile, or remain bound in the exciton. In TRMC, only free charge carriers contribute to the photoconductance. These free mobile charge carriers diffuse within the material and also gets transported to the transport layers. The concentration of photoexcited mobile electrons and holes are initially same. Their concentration decays with time and this depends on its recombination pathway which are discussed below:

- Radiative recombination - It is the recombination of free holes and electrons. It is radiative in nature resulting in a photoluminescence emission. The rate of radiative recombination depends on the number of holes and electrons. Hence, it is a second order decay.
- Shockley Read-Hall recombination - It is a nonradiative recombination taking place by means of trapping. It can be either an electron trap or a hole trap hence this rises to an unequal decay characteristic between the holes and electrons. It is a first order trap depending on the concentration of the empty traps and concentration of free charge carrier which can be trapped. The trapped charge carrier doesn't contribute to the photoconductance.
- Auger recombination - It is a non radiative recombination of third order. It is of importance when the generated charge carrier concentration is very high due to heavy doping or strong excitation of the material.

The presence of dark charge carrier i.e. the charge carriers which are present in the thermal equilibrium doesn't contribute to the photoconductance. It does affect the decay though as the concentration

of dark charge carriers (majority charge carrier) is quite large in comparison to the minority charge carrier affecting the second order radiative term.

For modelling the TRMC data for MAPI, the following things were assumed [54]:

- Homogeneous generation of charges throughout by a excitation wavelength close to the absorption onset.
- The exciton binding energy of MAPI is quite low and comparable to the thermal energy at room temperature ($k_B T$). So, all the absorbed photons leads to the formation of one free electron and hole.
- MAPI is a p-type material. So, the majority charge carrier is the hole.
- The mobility of the charge carrier is constant during the measurement time and independent of the concentration of the charge carriers

Now, the concentration of the charge carriers in the perovskite material can be modelled by the following differential equations (mentioned in [54] and based on Figure 3.6a:

$$\frac{dn_{CB}}{dt} = \frac{dn_e}{dt} = G_c - k_2 n_e(n_h + p_0) - k_T n_e(N_T - n_t) \tag{3.7}$$

This for the change in concentration for electrons (n_e) with time. G_c is the generation term. The second term represents the band to band recombination with a rate constant of k_2 whereas the third term is the first order (k_T) trap filling rate constant. n_h, p_0, N_T and n_T are the concentration of photo generated holes, dark carriers (holes, in this case), total traps and filled up traps (trapped charge carriers) respectively.

$$\frac{dn_{VB}}{dt} = -\frac{dn_h}{dt} = -G_c + k_2 n_e(n_h + p_0) + k_D n_t(n_h + p_0) \tag{3.8}$$

This equation is for the change in hole concentration with time. The term expresses trap depopulation or emptying where k_D is the rate constant for trap emptying. The concentration of filled traps mentioned in these equation can be expressed in terms of trap filling and depopulation as:

$$\frac{dn_t}{dt} = k_T n_e(N_T - n_t) - k_D n_t(n_h + p_0) \tag{3.9}$$

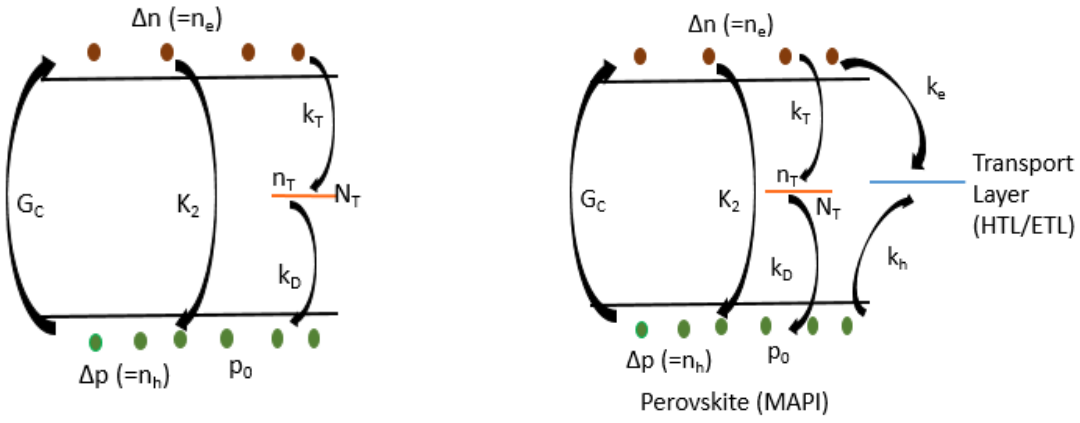

(a) Charge carrier dynamics in perovskite

(b) Charge carrier dynamics in perovskite and transport layers

Figure 3.6: Schematic of charge carrier dynamics

3.3.2. Modelling of Kinetics of Charges in MAPI with Transport Layers

When a transport layer is deposited on top of a perovskite material, the charge carriers can be extracted by the transport layer. Recombination via the interface can also take place as shown in Figure 3.6b. For instance, when C60 is deposited on top of MAPI, the electrons are extracted by C60 and some of them can also recombine with holes via the interface. The opposite happens when Spiro-MeOTAD is deposited as it is a hole transport layer. Charge extraction is a first order process. Depending on the selectivity of the transport layer, the charge transport rate constant of holes (k_h) and electrons (k_e) vary. In case of C60, k_e is quite large in comparison to k_h , which is in contrary to Spiro-MeOTAD as holes are extracted in the latter.[55]

These charge carriers dynamics can be expressed by the following differential equation which are analogous to the above equations.

$$\frac{dn_{CB}}{dt} = \frac{dn_e}{dt} = G_c - k_2 n_e(n_h + p_0) - k_T n_e(N_T - n_t) - k_e n_e \tag{3.10}$$

$$\frac{dn_{VB}}{dt} = -\frac{dn_h}{dt} = -G_c + k_2 n_e(n_h + p_0) + k_D n_t(n_h + p_0) + k_h n_h \tag{3.11}$$

$$\frac{dn_t}{dt} = k_T n_e(N_T - n_t) - k_D n_t(n_h + p_0) \tag{3.12}$$

$$\frac{dn_{TM}}{dt} = k_e n_e - k_h n_h \tag{3.13}$$

The last equation is for modelling the concentration of charge carriers which are extracted by the transport layer with respect to time.

4

Results and Discussions

4.1. Structural and Optical Properties of MAPI and Transport Layers

The XRD measurement on pristine MAPI and also with C_{60} and Spiro-MeOTAD was done using the Co kα beam. The result obtained is shown in Figure 4.1 . It is compared to the XRD measurement of literature and was found to be nearly accurate as shown in Table 4.1. The small peak at around 15° indicates the presence of PbI_2. The XRD measurement of MAPI with the transport layers, as shown in Figure A.1 also exhibit peaks at the same position. This means that the deposition of the transport layer doesn't affect the crystalline structure of MAPI.

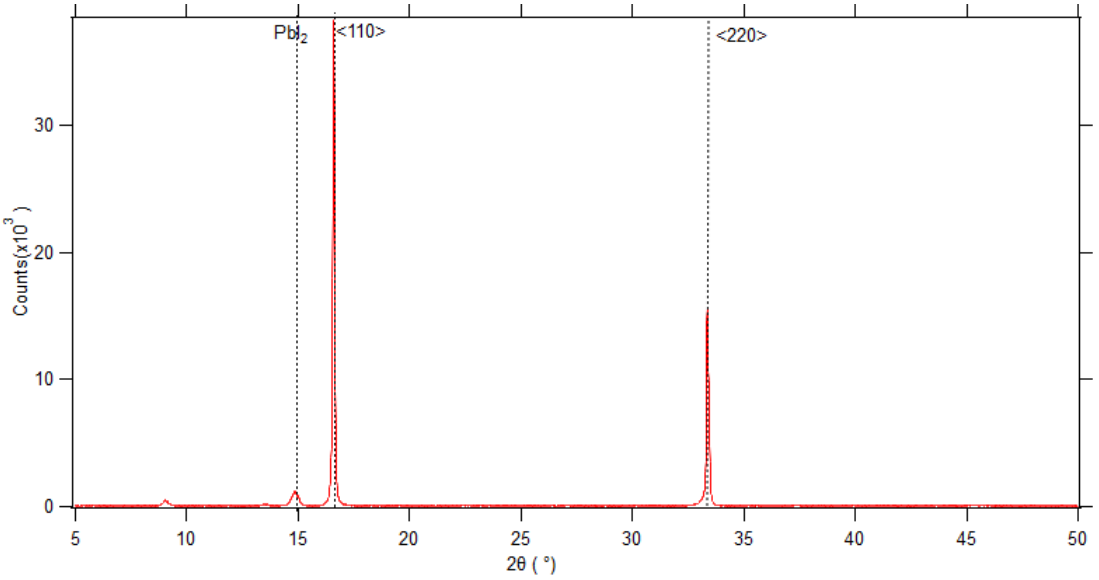

Figure 4.1: XRD of pristine MAPI

Table 4.1: Comparison of 2-θ angle obtained from XRD measurement and literature

	2-θ (°)	
Measured (Co kα)	16.5	33.5
Calculated (Cu kα)	14.16	28.38
Literature (Cu kα)[56]	14.0	28.36

The thickness of MAPI film was found to be 250±10nm. A thickness of 32±1nm was measured for C_{60} while that detected by the sensor of the evaporator was 30nm. The thickness of Spiro-MeOTAD was measured to be 232±12nm.

The fraction of absorbed light was calculated from the absorption measurement. It is shown in Figure 4.2 as a function of excitation wavelength of light. The band gap was approximated to 1.615eV from the Tauc plot as shown in Figure A.4. The fraction of absorbed light at 650nm when light first passes from the side of quartz ('backside') is shown in Table 4.2. This wavelength is used for excitation in the TRMC measurements and the fraction of absorbed values are used further in the study.

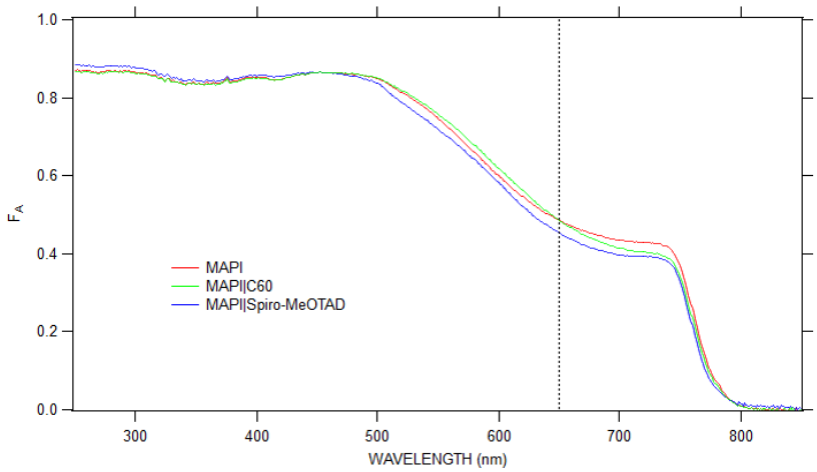

Figure 4.2: Absorption of pristine MAPI and with C_{60} and Spiro-MeOTAD as the transport layers by backside measurement

Table 4.2: Absorption of pristine MAPI and MAPI with C_{60} and Spiro-MeOTAD at 650nm by backside measurement

Material	**Fraction absorbed**
MAPI	0.4952
MAPI | C_{60}	0.4953
MAPI | Spiro-MeOTAD	0.4531

The fractions of absorbed light by Spiro-MeOTAD and C_{60} at 650nm were found to be 0.0118 and 0.0031 respectively and negligible as compared to the MAPI. An absorption measurement from the frontside i.e. illumination from the direction of the films were done and is shown in Figure A.2 along with the fraction reflected data (Figure A.3).

The PL intensity of MAPI was found to be centered at 760nm when excited by a red laser (wavelength ~635nm). The PL intensity was quenched as shown in Figure 4.3 for MAPI with the transport layers. As the intensity of the PL is proportional to the amount of radiative recombination, the quenching of the PL intensity was indicative of an effective charge extraction by the HTL or ETL thereby decreasing the amount of holes or electrons in the MAPI for radiative recombination.

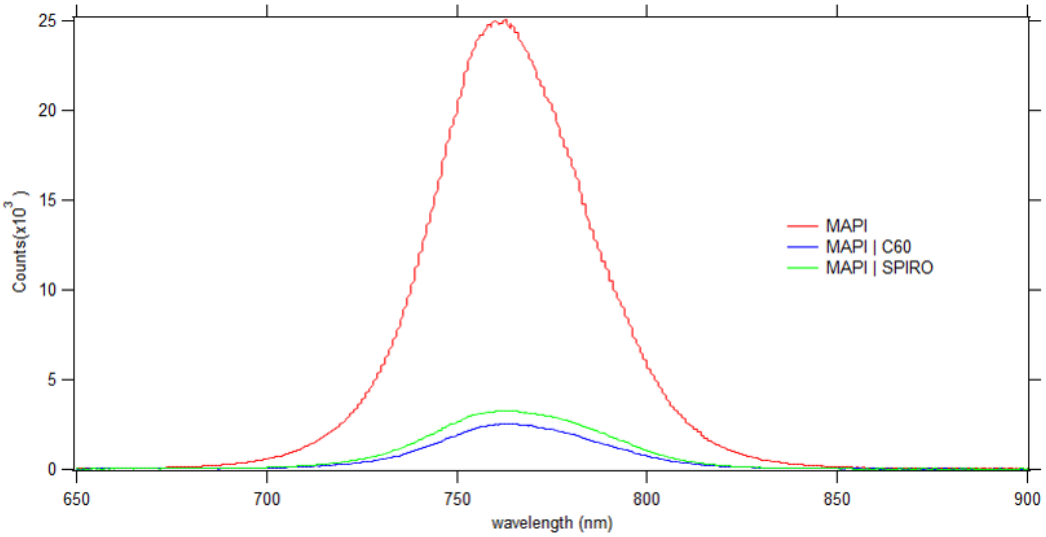

Figure 4.3: Steady state PL of pristine MAPI and with C_{60} ETL and Spiro-MeOTAD HTL

4.2. Opto-electronic Properties of MAPI and Transport Layers

The TRMC measurements were done under varying laser intensity ranging from 10^8 to 10^{12} photons/cm^2 with open cell for higher photon fluence and cavity for lower photon fluence due to the increased sensitivity. When a frequency scan is done, a decrease in the reflected power (referred as ”dip”) is seen at point where the interaction of the microwave with the charge carriers is maximum due to resonance. All the TRMC measurements are done at this resonant frequency. The TRMC measurement as shown in Figure 4.4 has a sharp increase upon excitation in the photo-conductance normalised by the fraction of absorbed light, intensity, electric charge and the ratio of wide and small inner walls of microwave guide. This is due to the free charges created by the laser pulse. It is followed by a decay in the photo-conductance as the number of charge carrier decreases due to trapping or band to band recombination.

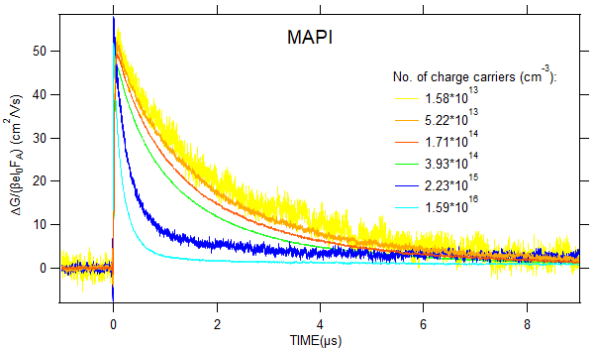

(a) TRMC trace for MAPI

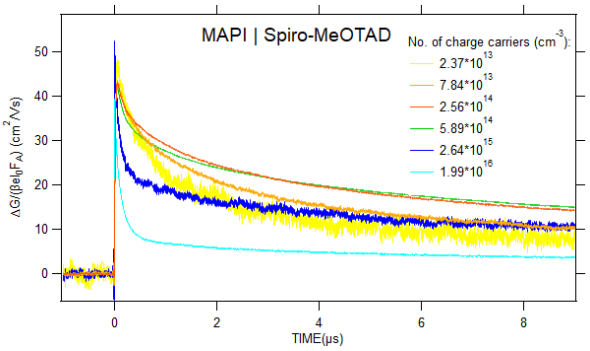

(b) TRMC trace of MAPI | Spiro-MeOTAD

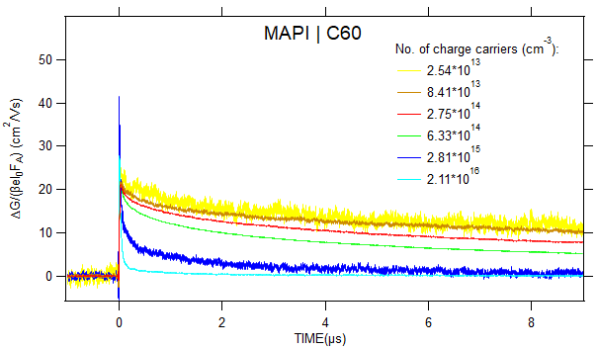

(c) TRMC trace of MAPI | $_{60}$

Figure 4.4: TRMC traces of MAPI, MAPI | Spiro-MeOTAD and MAPI | C_{60} when excited at 650nm from backside.

As compared to pristine MAPI, the lifetime of charge carriers in MAPI with a transport layer is more as shown in Figure 4.5. This is understood by the slower decay of the traces. The generated charges move to the HTL or ETL. For instance in the MAPI|C_{60} bilayer system, the electron moves to the ETL leaving behind the hole in MAPI. This slows down the recombination of electrons with the holes present in MAPI resulting in a longer lifetime. Apart from trapping and band to band recombination, interfacial recombination of the electron hole pair also contributes to the decay in the signal of the MAPI with the transport layers.

Curve fitting of the TRMC traces of pristine MAPI and with C_{60} and Spiro-MeOTAD were done in Igor according to the differential equations present in Section 3.3 and is shown Table 4.3. The thickness of the MAPI layer was only considered as the absorption by the transport layers at this wavelength were negligible.

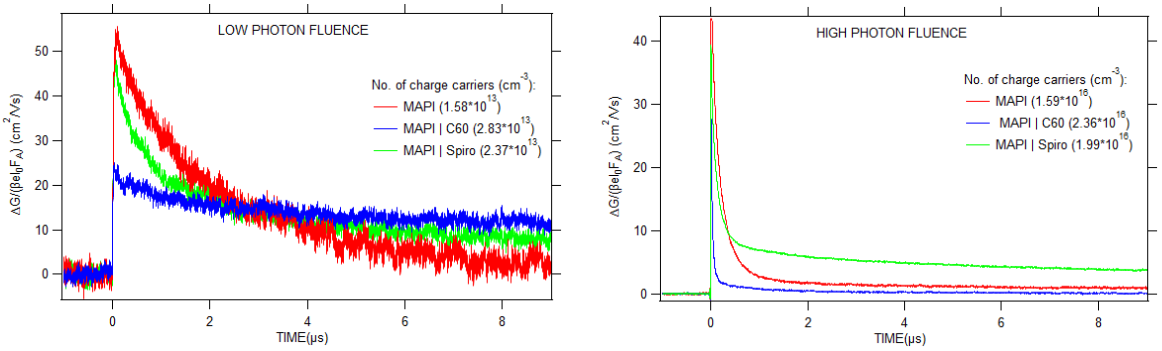

(a) Comparison at Low Photon Fluence

(b) Comparison at High Photon Fluence

Figure 4.5: TRMC trace of MAPI with Spiro-MeOTAD and C_{60}

Table 4.3: Kinetic parameters derived from curve fitting of TRMC traces of MAPI and MAPI with C_{60} and Spiro-MeOTAD

Parameters	**MAPI**	**MAPI | C_{60}**	**MAPI | Spiro-MeOTAD**
k_t ($*10^{-8}$ cm^3s^{-1})	1	1.2	0.8
k_2 ($*10^{-9}$ cm^3s^{-1})	2	6	1.2
k_D ($*10^{-8}$ cm^3s^{-1})	1	2	1
N_t ($*10^{14}$ cm^{-3})	1.4	1.4	0.7
k_e ($*10^6$ s^{-1})		4	0.008
k_h ($*10^6$ s^{-1})		0.06	5

The efficient transfer of the holes to the Spiro-MeOTAD layer and the electrons to the C_{60} can be seen from the high charge transfer rate and a small interface recombination rate. This results in the increase of the lifetime of charge carriers because recombination is slowed down as mentioned above.

The difference in the k_2 value between pristine MAPI and MAPI with transport layers can be due to photon reabsorption or photon recycling.[57] Photon recycling is the self absorption of the emitted photons by radiative recombination of holes and electrons. This effects the k_2 which is measured because it may show an apparent slower radiative recombination rate as the photon is trapped and may undergo multiple photon recycling process. The photon recycling is affected by the refractive index of the surrounding layer. So, the presence of the transport layer in the bilayer system can lead to the difference in the k_2.[58]

4.3. Effect of Bias Light

The set up used for studying the effect of Bias light on the dynamics of the charge carriers in MAPI and the ETL / HTL is described in subsection 3.2.4. At first, a TRMC measurement was done in the absence of bias light followed by a measurement in presence of bias light and lastly one in the absence of the bias light. The samples were excited from the backside i.e. from the side of the quartz substrate and its reverse side i.e. the front side. The measurements were done in both cavity and open cell. The results discussed below is based on backside measurement and at 95.68W/m^2 bias light power in cavity unless mentioned otherwise. The rise in temperature of the sample due to the heat produced by the incidence of the bias light during the experiment can be ignored as the rise in temperature is negligible as shown in Figure A.5. The photo-conductance vs time curves of the TRMC results were plotted. They were not normalised by the intensity as the intensity used by the software to generate the normalised photo-conductance curve takes into account only the laser intensity and not the intensity of the bias light.

4.3.1. Effect of Bias Light on MAPI and Transport layers

A frequency scan in the range of 8.2-12.2GHz was done on pristine MAPI and with the HTL/ETL and a decrease in the reflected microwave power is seen at the resonance point creating a ”dip”. In all the cases as shown in Figure 4.6, there is a dip deepening occurring in the illuminated condition under bias light as compared to the dark condition. This is indicative of the extra charges produced due to the steady state charge generation in presence of the bias light.

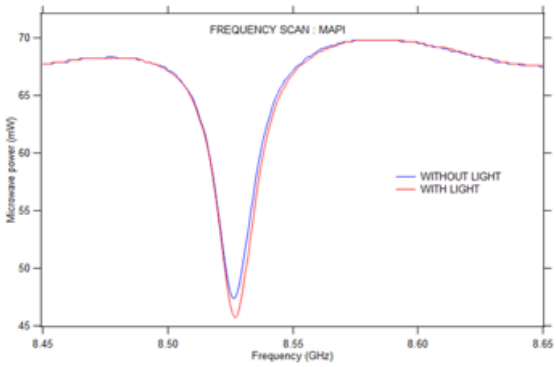

(a) Frequency scan of MAPI

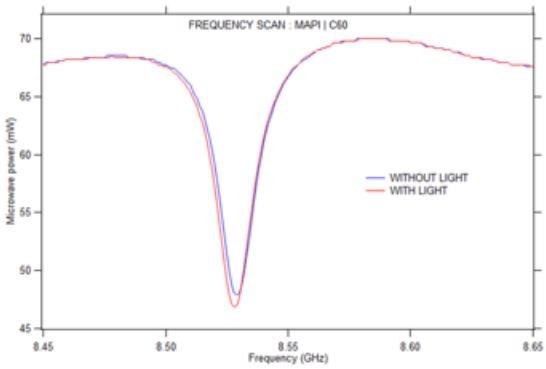

(b) Frequency scan of MAPI | C_{60}

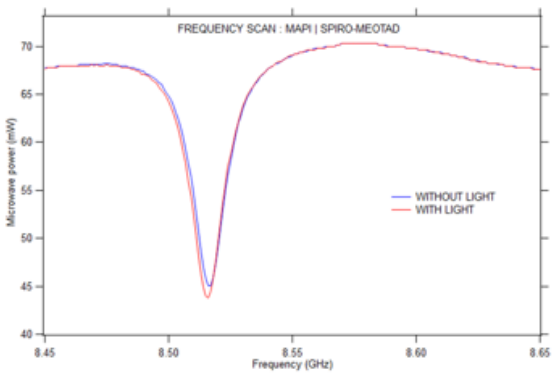

(c) Frequency scan of MAPI | Spiro-MeOTAD

Figure 4.6: Frequency scan measured at high bias intensity of 95.68W/m_2 from backside

The photo-conductance obtained from the TRMC measurement was used for the comparison to check the effect of the bias light. As shown in Figure 4.7, the decay of the TRMC signal of MAPI is slightly more when measured in dark again after illumination as compared to its initial condition in both at low and high photon fluence of the laser. Therefore, there is a decrease in the lifetime of the charge carriers after it had been illuminated. This can be due to the creation of traps by the white light. The photo-conductance measured in presence of the bias light has a lower intensity as compared to that in dark condition which is due to the time resolution of the cavity failing to capture the fast decay in the signal as shown in Figure A.7. This fast decay in the signal is due to the increased band to band recombination because of the huge number of charges produced in presence of the bias light. A similar result was obtained in case of the front side illumination as shown in Figure A.15.

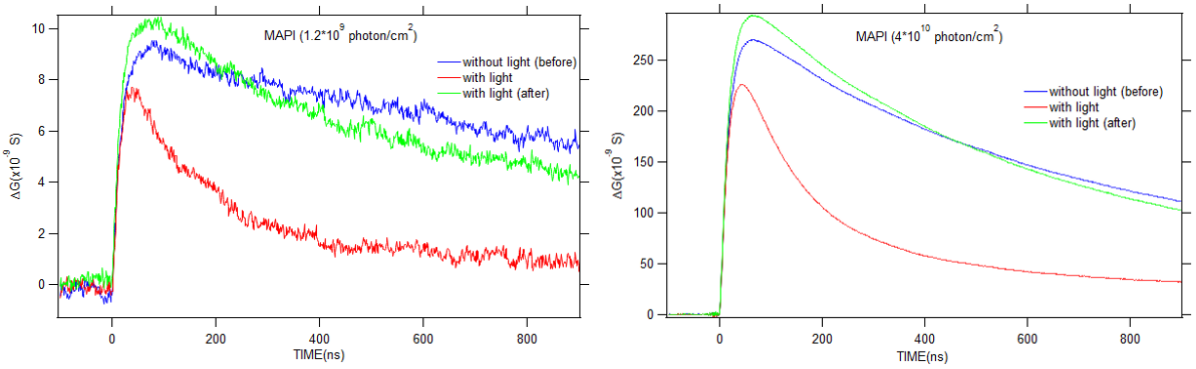

(a) Low photon fluence of laser

(b) High photon fluence of laser

Figure 4.7: Comparison of TRMC traces of MAPI with light and without light before and after illumination with white light

When MAPI with C_{60} as the ETL was illuminated there was an increase in decay of the TRMC signal which is due to the increase in the band to band recombination as there is more number of charge carriers present. However, at higher photon fluence as shown in Figure 4.9 it can be seen that the decay of MAPI | C_{60} becomes comparable to that of MAPI. This is not present in the lower photon fluence of the laser as shown in Figure 4.8 where the lifetime of the charge carriers is still more than pristine MAPI similar to the measurement conducted in the absence of the bias light. This is because as more charge carriers are generated, more electrons are transported to the C_{60}.This can affect the band bending at the interface of MAPI and C_{60} and the difference between the LUMO of the C_{60} layer and the conduction band of the MAPI can decrease. Here, no electrode are present to extract the electrons from the system. So, at higher photon fluence, C_{60} may get saturated with the electrons and no more electron can be transferred to it as there is no more potential to drive it to the ETL. The TRMC measurement, now, shows charge carrier dynamics in this bi-layer system similar to the pristine MAPI. So, the decay of the MAPI | C_{60} becomes comparable to MAPI under illumination as can also be seen in Figure A.11.

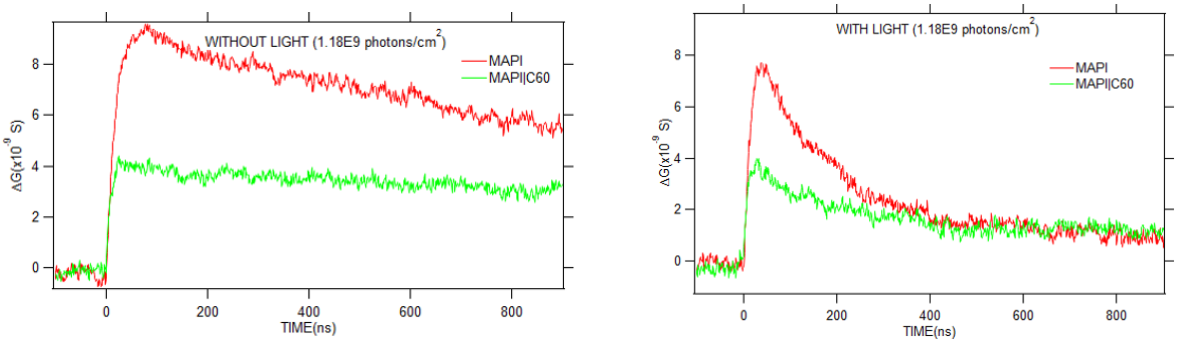

Figure 4.8: Low photon fluence of laser

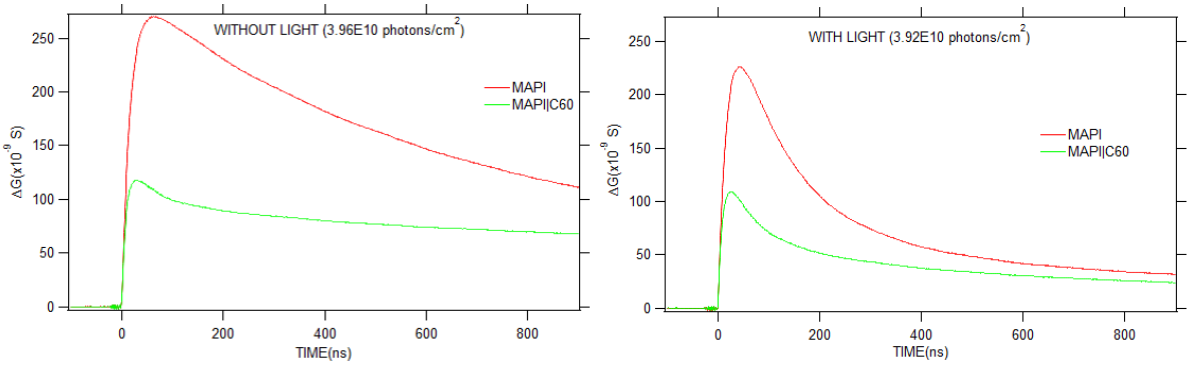

Figure 4.9: High photon fluence of laser

It can also be seen in Figure 4.10 that the lifetime of the charge carriers in absence of the continuous illumination after the bias light experiment reverts back to its original condition.
The front side measurement shown in Figure A.13 also yielded a similar result.

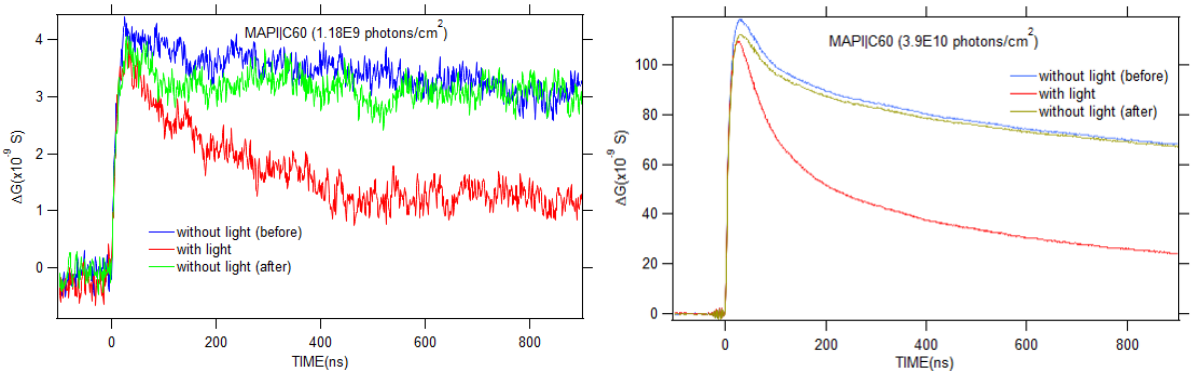

(a) Low photon fluence of laser

(b) High photon fluence of laser

Figure 4.10: Comparison of TRMC traces of MAPI | C_{60} with light and without light before and after illumination with white light

When MAPI with Spiro-MeOTAD layer was illuminated, a sample degradation was observed in both cases of frontside and backside illumination as shown in Figure 4.11 and Figure 4.12. This could be understood from the decay of the TRMC traces after the bias light experiment. The traces doesn't show a similar characteristics as the original traces. A difference in the TRMC traces of the degraded samples after it had been illuminated from the frontside and backside can be seen. One of the possible reason for the higher degradation on illumination from the frontside can be that the interface is illuminated more when it is illuminated from this direction as absorption by Spiro-MeOTAD is negligible whereas in backside illumination, light is first absorbed by the MAPI layer. It had been seen in previous studies that migration of halide ions take place away from the illuminated region.[51] So, the interface is affected more in the former case as more defects may have formed there.

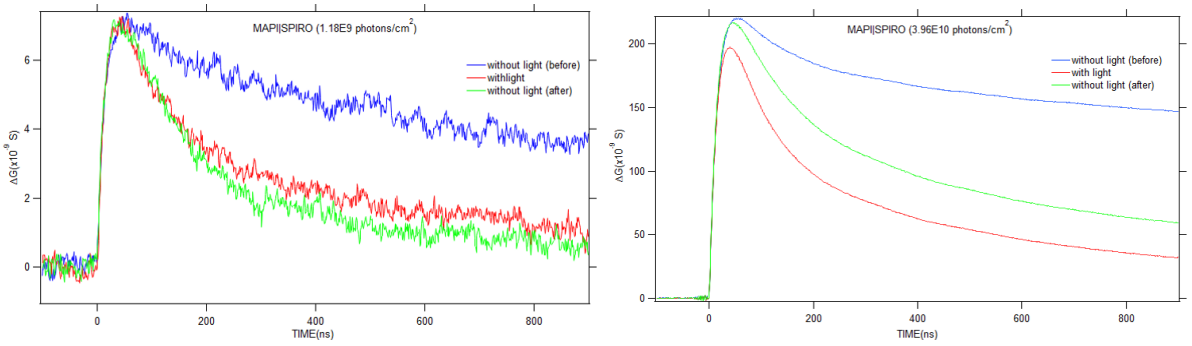

(a) Low photon fluence of laser

(b) High photon fluence of laser

Figure 4.11: Comparison of TRMC traces of MAPI | Spiro-MeoTAD with light and without light before and after illumination with white light when measured from backside

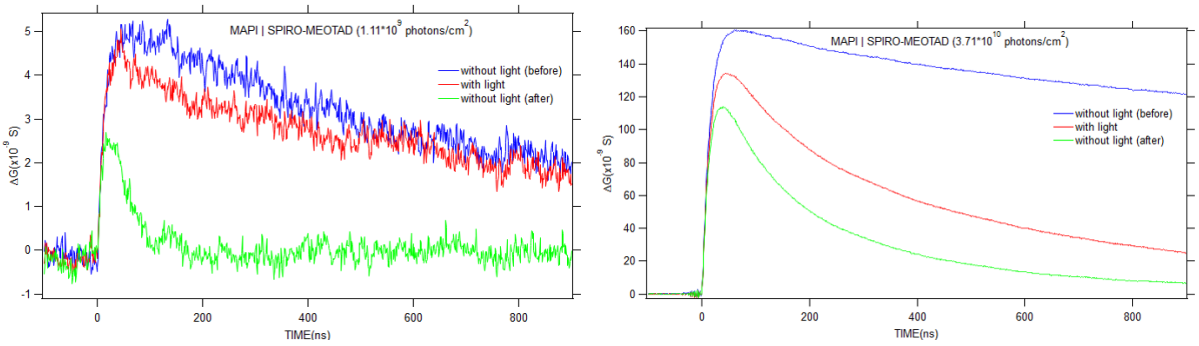

(a) Low photon fluence of laser

(b) High photon fluence of laser

Figure 4.12: Comparison of TRMC traces of MAPI | Spiro-MeoTAD with light and without light before and after illumination with white light when measured from frontside

The decay of Spiro-MeOTAD layer is seen to be similar to that of MAPI as shown in Figure 4.13 and Figure 4.14. However, the fast decay can be an effect of the degradation too. So, it is not possible to tell whether the Spiro-MeOTAD layer gets saturated or not.

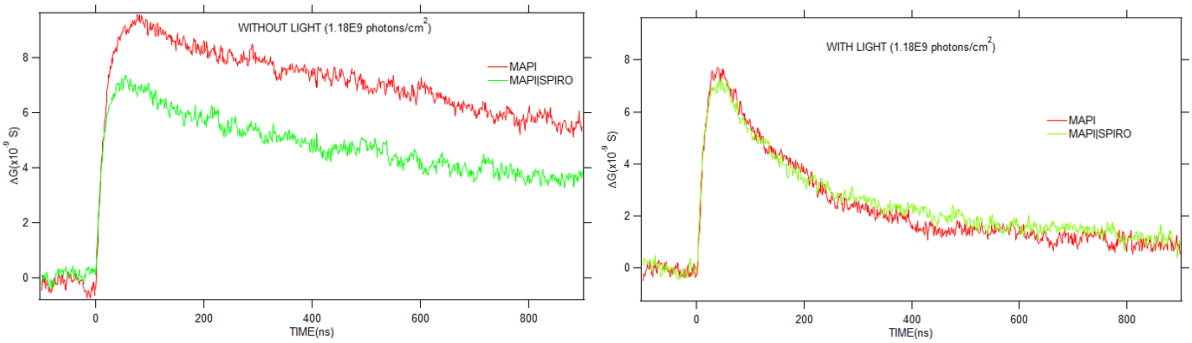

Figure 4.13: Continuous excitation of MAPI|Spiro-MeOTAD from the backside : Low photon fluence of laser

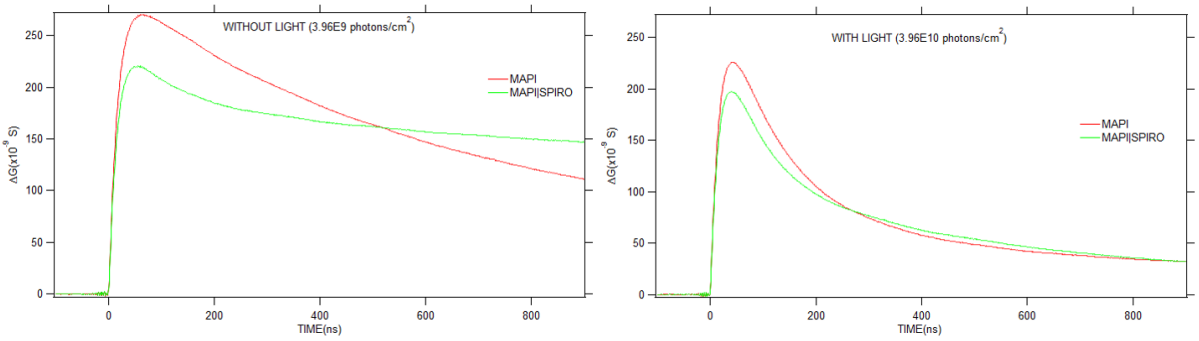

Figure 4.14: Continuous excitation of MAPI|Spiro-MeOTAD from the backside : High photon fluence of laser

However, when illuminated from the front side, saturation of the Spiro-MeOTAD layer by holes doesn't take place as shown in Figure 4.15 and Figure 4.16. Degradation of the MAPI|Spiro-MeOTAD takes place as shown above. So, this can affect the hole transfer and hence the TRMC traces.

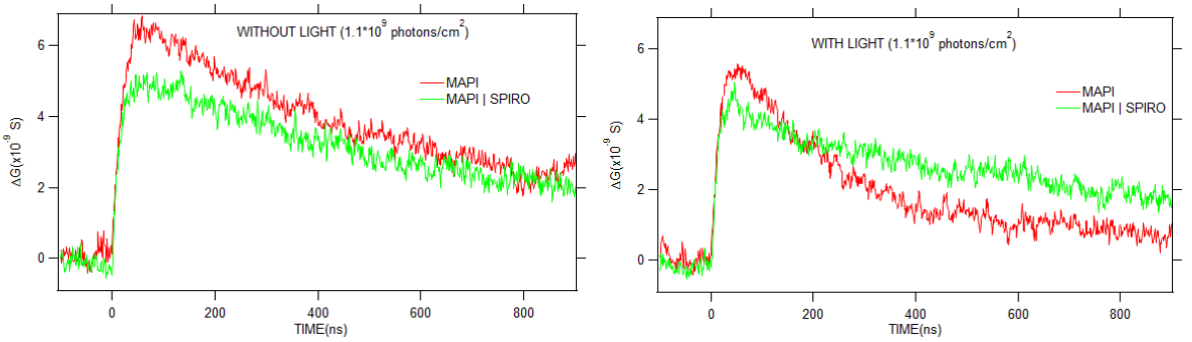

Figure 4.15: Continuous excitation of MAPI|Spiro-MeOTAD from the frontside : Low photon fluence of laser

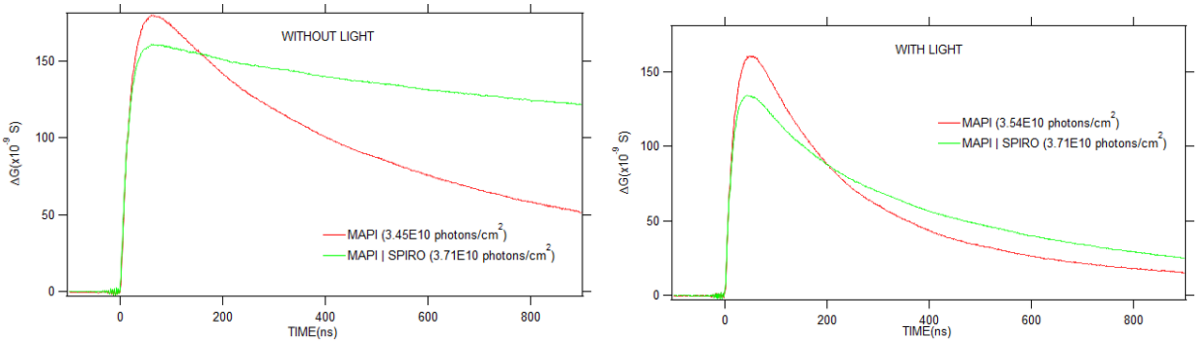

Figure 4.16: Continuous excitation of MAPI|Spiro-MeOTAD from the frontside : High photon fluence of laser

It is suspected that the main reason behind the degradation of the MAPI | Spiro-MeOTAD is migration of ions which in turn creates defects in the interface. At low temperature, ion mobility decreases. So, a study at low temperature is done next to understand the effect of temperature on the charge carrier dynamics in presence of bias light.

4.3.2. Effect of Temperature and Bias Power

The measurements were done in the (cavity) temperature cell where the temperature inside the cell was maintained at 200K (-73°), so that the ion migration decreases but the tetragonal state of MAPI is retained. The measurements had to be done at a low intensity of 13.16W/m^2 from the LED source in order to accommodate the temperature cell in the set up. All the measurements were done here by illuminating pristine MAPI and MAPI with Spiro-MeOTAD from the front side.

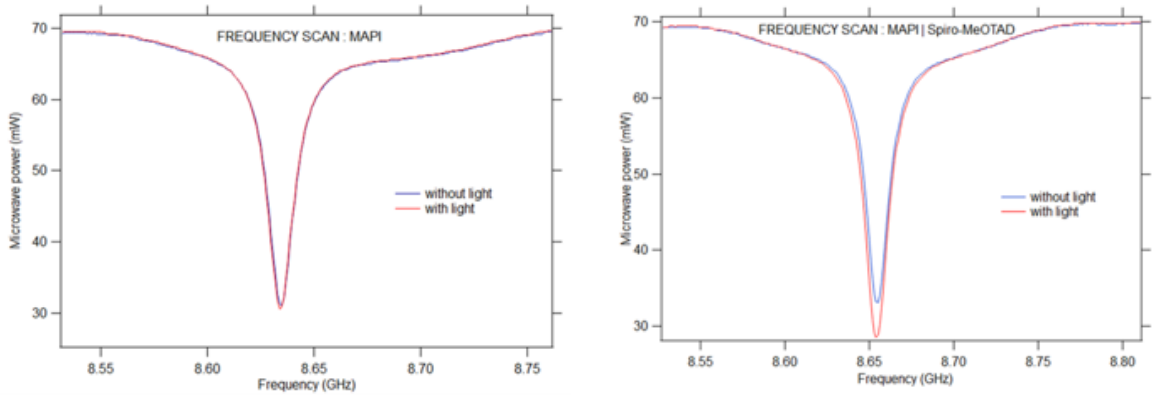

(a) Frequency scan of MAPI

(b) Frequency scan of MAPI | Spiro-MeOTAD

Figure 4.17: Frequency scan measured at low bias power at 200K from frontside

A dip deepening was not observed in the frequency scan of pristine MAPI as shown in Figure 4.17. It was also not observed when it was measured at this low bias intensity at room temperature as shown in Figure A.14. So, this could be due to the much less charges generated at this power. However, the dip deepening was observed in MAPI | Spiro-MeOTAD as shown in Figure 4.17. It was also observed at a similar condition at room temperature.

When the pristine MAPI was illuminated there was an increase in decay as shown in Figure 4.18 which is because of the increased band to band recombination due to the excess charge carriers formed. The decay was not as fast as the one present at higher bias power which can be due to the lesser number of charge carriers produced. The lifetime decreased from the initial condition when measuring it after the bias light experiment in dark. This is similar to when the experiment was conducted at the high bias power.

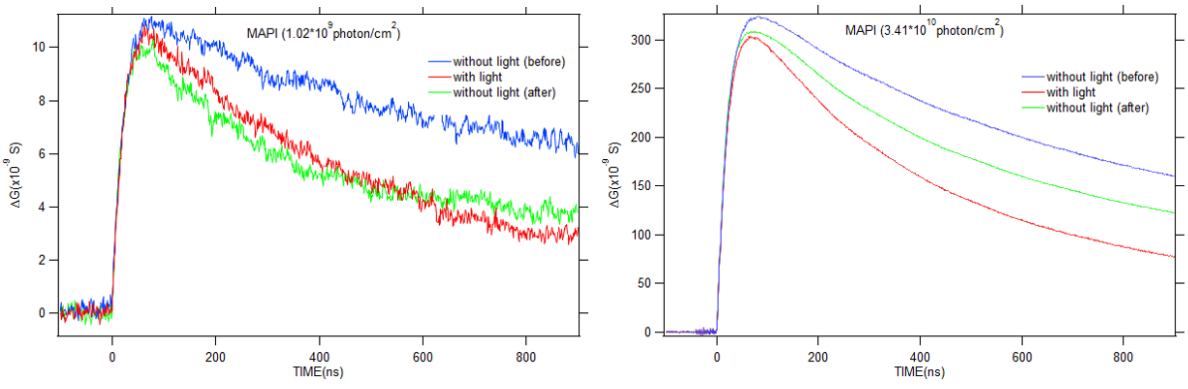

(a) Low photon fluence of laser

(b) High photon fluence of laser

Figure 4.18: Comparison of TRMC traces of MAPI with light and without light before and after illumination with white light

When the MAPI with Spiro-MeOTAD bilayer was illuminated, degradation didn't take place as shown

in Figure 4.19. So, it is possible that the interface of the MAPI - Spiro-MeOTAD is not affected here.

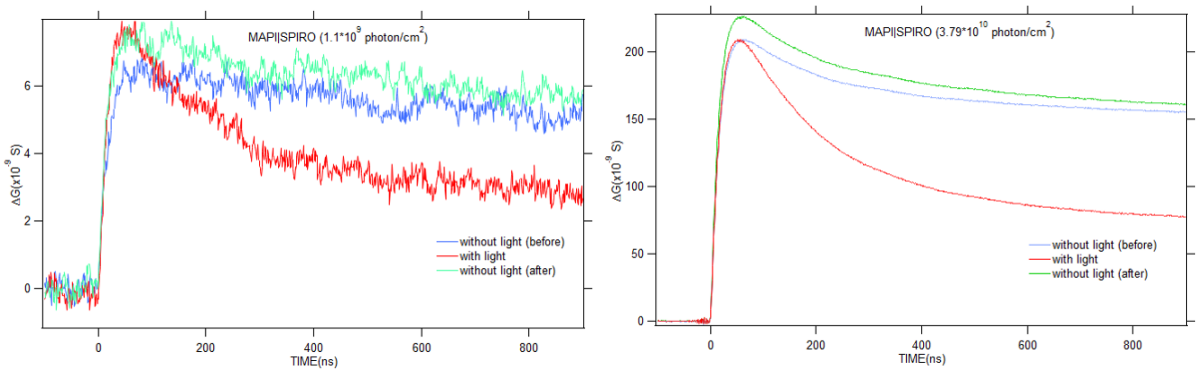

(a) Low photon fluence of laser

(b) High photon fluence of laser

Figure 4.19: Comparison of TRMC traces of MAPI | Spiro-MeOTAD with light and without light before and after illumination with white light at low bias intensity at 200K

However, in this experimental condition, the saturation of Spiro-MeOTAD doesn't take place. It can be seen in Figure 4.21 that even at high photon fluence of the laser, the decay of the MAPI | Spiro-MeOTAD doesn't become comparable to the MAPI. This can be due to the usage of low bias power leading to the generation of lesser number of charge carriers as compared to the high bias power. The holes get extracted by the Spiro-MeOTAD layer which can be understood by the increase in lifetime of the charge carriers as compared to the pristine MAPI.

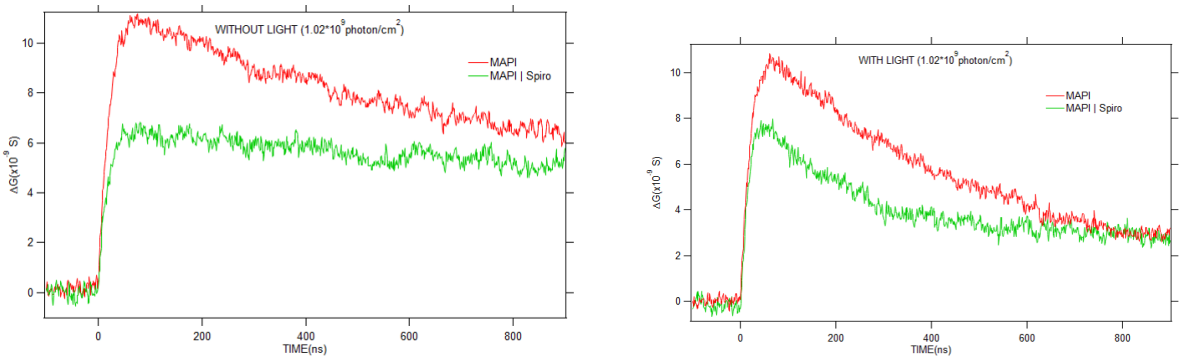

Figure 4.20: Continuous excitation of MAPI|Spiro-MeOTAD from the frontside at low bias power at 200K : Low photon fluence of laser

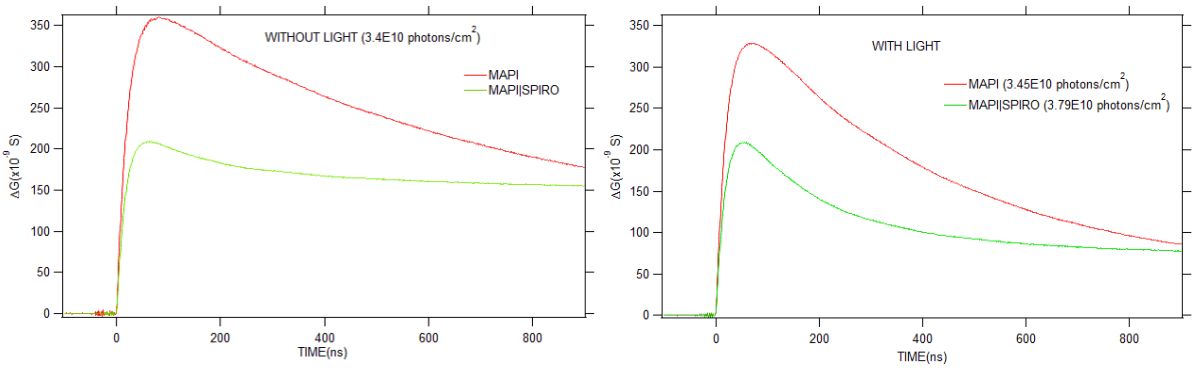

Figure 4.21: Continuous excitation of MAPI|Spiro-MeOTAD from the frontside at low bias power at 200K : High photon fluence of laser

Next, the measurements were done at a room temperature but at the same low bias intensity of 13.16W/m^2. This was done to check whether the degradation of the MAPI | Spiro-MeOTAD was caused due to the higher bias intensity of the previous setup or it is temperature dependent. As shown in Figure 4.22, it can be seen that there is an increased decay in the MAPI | Spiro-MeOTAD resulting in a decreased lifetime of the charge carriers. This, thus, proves that the suggested reason behind the degradation is true. The ion migration creates defects and affects the MAPI HTM interface. Decrease in temperature decreases ion mobility. In this low temperature due to no/ negligible ion migration, degradation is prevented.
The decay of the TRMC signal of MAPI | Spiro-MeOTAD in the presence of continuous illumination is not as much as that present in the high bias power. This can be due to lesser number of charge carriers generated because of the lower bias power resulting in reduced band to band recombination. It was previously seen in Figure 4.4b, that the lifetime of the charge carriers in MAPI|Spiro-MeOTAD increased as the photon fluence increased as more number of charge carriers were extracted by the HTL followed by an increase in decay with increase in photon fluence as band to band recombination increases. Here, too, a similar effect is seen when the photon fluence of the laser is less. On continuous illumination the lifetime increases but when there is a high photon fluence of the laser, the decay increases due to band to band recombination.

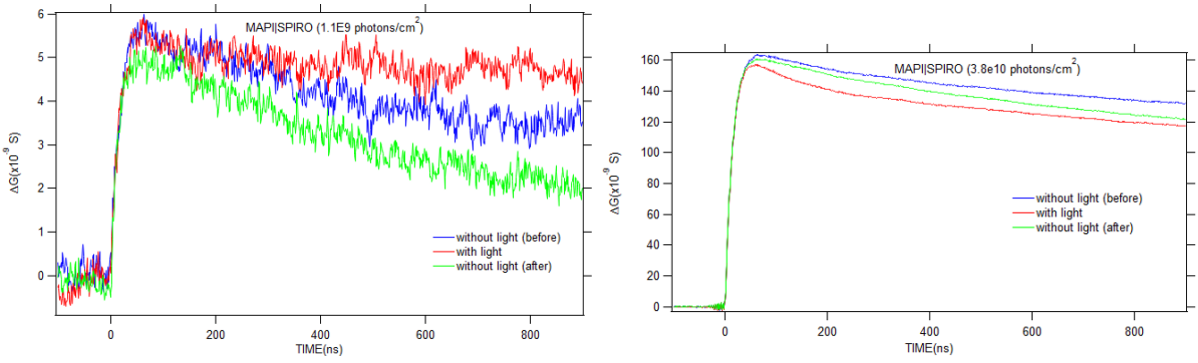

(a) Low photon fluence of laser

(b) High photon fluence of laser

Figure 4.22: Comparison of TRMC traces of MAPI | Spiro-MeOTAD with light and without light before and after illumination with white light at low bias intensity at room temperature

Similar to the measurement in the low temperature, here too the saturation of the Spiro-MeOTAD layer doesn't take place even at high photon fluence of the laser as seen in Figure 4.23 and Figure 4.24. The lifetime of the charge carriers in the bilayer system was more than that of pristine MAPI. So, it can be said that at low bias intensity the Spiro-MeOTAD layer can't be saturated as enough charges are

not continuously generated.

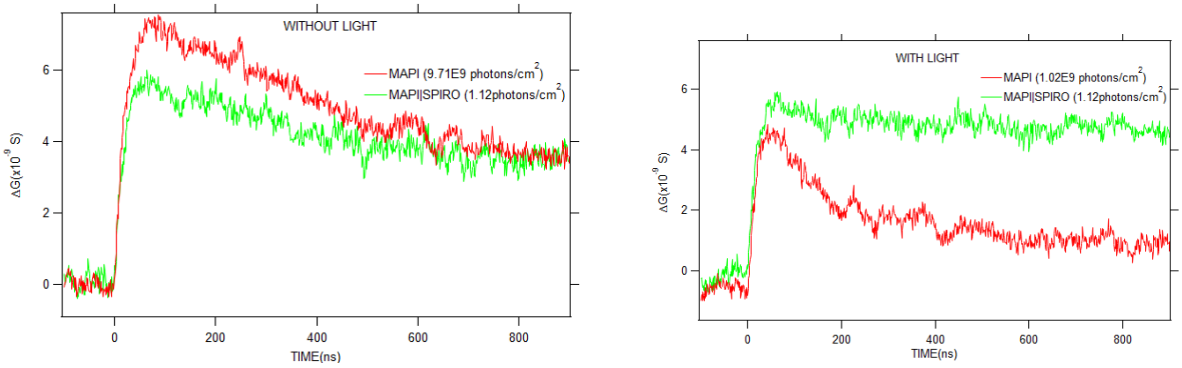

Figure 4.23: Continuous excitation of MAPI|Spiro-MeOTAD from the frontside at low bias power at room temperature : Low photon fluence of laser

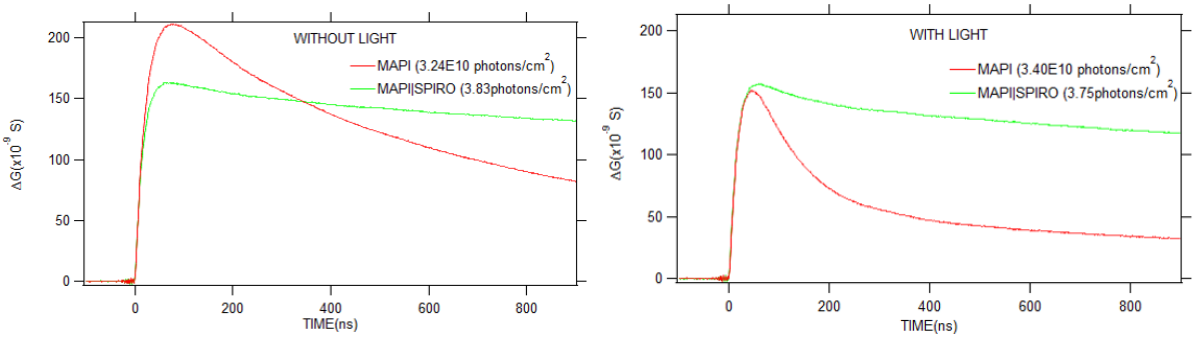

Figure 4.24: Continuous excitation of MAPI|Spiro-MeOTAD from the frontside at low bias power at room temperature : High photon fluence of laser

4.3.3. Modelling of TRMC traces

Table 4.4: Kinetic parameters derived from curve fitting of TRMC of MAPI

Parameters	before	after	before	after	before	after
	MAPI		MAPI | C_{60}		MAPI | Spiro-MeOTAD	
$\Sigma\mu$ (cm^2/Vs)	120	125	120	125	120	125
k_2 ($*10^{-9}$ cm^3s^{-1})	2	0.4	6	6	1.2	1
N_t ($*10^{14}$ cm^{-3})	1.4	2.7	1.4	2.7	0.7	2.7
p_0 ($*10^{13}$ cm^{-3})	2	0.9	2	0.9	2	0.9
k_e($*10^6s^{-1}$)			4	4	0.008	0.2
k_h($*10^6s^{-1}$)			0.06	0.06	5	3

It can be seen from Table 4.4 that the number of traps doubles in MAPI and MAPI | C_{60} after the bias light experiment.The increase is neary four times in MAPI | Spiro-MeOTAD. This can be due to the defects created by ion migration. It can also be seen that the defects created doesn't affect the charge extraction by the C_{60} layer. This can mean that the defects or trap states are not created in the interface between MAPI | C_{60}. Whereas, it can be seen that the hole transport rate constant decreases and interfacial recombination increases in the MAPI | Spiro-MeOTAD bilayer system. This can be due to the creation of defects in the interface increasing the interfacial recombination.
The change in the value of k_2 in MAPI can be due to photon reabsorption. The number of times the

photon is absorbed and emitted in this photon recycling can be expressed as :

$$N_{PR} = \frac{\delta}{\sqrt{{L_D}^2 + {L_\alpha}^2}} \tag{4.1}$$

where, δ is the mean depth of carrier, L_D distribution is the carrier diffusion length and L_α is the photon propagation length.[59] As the number of traps are increasing in the pristine MAPI after illumination, the carrier diffusion length decreases. This can affect the number of times the photon recycling is taking place due to which the k_2 value is different from the initial condition. The change is not observed in the bilayer system. This can be due to the differnce in the refractive index as mentioned in Section 4.2.

5

Conclusion and Recommendation

5.1. Conclusions

Firstly, it can be concluded that the charge transfer from the MAPI perovskite layer to the C_{60} electron transport layer and Spiro-MeOTAD hole transport layer is efficient. This could be understood from the increase in the lifetime of the charge carriers in the bilayers due to charge extraction as compared to the monolayer pristine perovskite. The PL also shows a quenching of the intensity in the bilayers proving the same. The curve fitting of the TRMC traces also showed that there is a high electron transfer rate constant of $4*10^6 s^{-1}$ to the C_{60} and hole transfer rate constant of $5*10^6 s^{-1}$ to the Spiro-MeOTAD layer.

In presence of bias illumination, there was a possible saturation of the C_{60} at high photon fluence on excitation from both frontside and backside due to the increased number of free charges produced under continuous illumination. After continuous illumination, when the bilayer system was excited by the pulsed laser, there was no change in the electron transfer rate to the C_{60} but a small change in the hole transfer rate was observed from the MAPI to the Spiro-MeOTAD HTL. An increase in the mobility was also seen. It is not possible to conclude whether saturation of Spiro-MeOTAD layer took place or not due to the degradation of the sample. The interfacial recombination at the interface of MAPI | C_{60} had a slight increase after the continuous bias illumination experiment as compared to the MAPI | Spiro-MeOTAD which underwent a huge change. This could mean that the interface of the MAPI | C_{60} is not affected by continuous illumination and no/negligible trap states are created there.

Another thing that we had observed was the increase in the number of traps in the pristine MAPI and also in the bilayer systems. In pristine MAPI and with the C_{60}, the number of traps nearly doubles. It severely affects the charge carrier dynamics in MAPI | Spiro-MeOTAD bilayer system as the number of traps increases nearly fourfold here. As mentioned before, the interfacial recombination of the holes with the electrons takes place at a much higher rate than before which can mean that traps are formed near the interface and cause the degradation of this bilayer system. These traps prevent proper transfer of holes from the MAPI to the Spiro-MeOTAD and this could lead to a decrease in the open circuit voltage. It was suspected that these traps were caused by migration of ions as had been reported in the literature. So, a low temperature measurement was done to check this claim. It was seen that this degradation was no more seen in MAPI | Spiro-MeOTAD. So, it can be concluded that the mobile ions can create defects.

5.2. Recommendations

The following recommendations have been made based on the results of the experiments that we had conducted, the limitations present and additional ideas related to it.
Firstly, it was seen that there is some creation of traps after light is shone. The kind of traps created can be characterised and ways to passivate them can be found it. It can be further investigated whether they are successful in preventing degradation and their effect on the saturation of the transport layer on bias illumination.

Secondly, the number of charge carriers generated on bias light illumination is not calculated here. This can be found out by the curve fitting of the frequency scan. This value is quite accurate and can be compared to the number of charge carriers calculated from the TRMC traces on laser excitation with bias light.
Thirdly, the effect of low power on MAPI | C_{60} has not been investigated here and this can be done in the future. It had been studied in the literature that different wavelengths of lights have different effect. Its effect on the charge carrier dynamics can be studied by using light from monochromatic LED. Lastly, lead is toxic in nature and currently in various research it is being replaced by triple cation perovskite like $Cs_2AgBiBr_6$. The charge carrier dynamics can be studied on these materials as it is more sustainable. Moreover, different transport layers can also be used and the effect of bias illumination on the charge dynamics can be studied there.

Bibliography

[1] J. Cui, H. Yuan, J. Li, X. Xu, Y. Shen, H. Lin, and M. Wang, "Recent progress in efficient hybrid lead halide perovskite solar cells," *Science and technology of advanced materials*, vol. 16, no. 3, p. 036 004, 2015.

[2] *Best research-cell efficiency chart*. [Online]. Available: `https://www.nrel.gov/pv/cell-efficiency.html`.

[3] P. Roy, N. K. Sinha, S. Tiwari, and A. Khare, "A review on perovskite solar cells: Evolution of architecture, fabrication techniques, commercialization issues and status," *Solar Energy*, vol. 198, pp. 665–688, 2020.

[4] X. Tong, F. Lin, J. Wu, and Z. M. Wang, "High performance perovskite solar cells," *Advanced Science*, vol. 3, no. 5, p. 1 500 201, 2016.

[5] F. Di Giacomo, V. Zardetto, G. Lucarelli, L. Cinà, A. Di Carlo, M. Creatore, and T. Brown, "Mesoporous perovskite solar cells and the role of nanoscale compact layers for remarkable all-round high efficiency under both indoor and outdoor illumination," *Nano Energy*, vol. 30, pp. 460–469, 2016.

[6] D. Zhou, T. Zhou, Y. Tian, X. Zhu, and Y. Tu, "Perovskite-based solar cells: Materials, methods, and future perspectives," *Journal of Nanomaterials*, vol. 2018, 2018.

[7] *Perovskites solar cell structure, efficiency amp; more*. [Online]. Available: `https://www.ossila.com/pages/perovskites-and-perovskite-solar-cells-an-introduction`.

[8] N.-G. Park, "Perovskite solar cells: An emerging photovoltaic technology," *Materials today*, vol. 18, no. 2, pp. 65–72, 2015.

[9] F. G. Santomauro, J. Grilj, L. Mewes, G. Nedelcu, S. Yakunin, T. Rossi, G. Capano, A. Al Haddad, J. Budarz, D. Kinschel, *et al.*, "Localized holes and delocalized electrons in photoexcited inorganic perovskites: Watching each atomic actor by picosecond x-ray absorption spectroscopy," *Structural Dynamics*, vol. 4, no. 4, p. 044 002, 2017.

[10] C. Li, X. Lu, W. Ding, L. Feng, Y. Gao, and Z. Guo, "Formability of abx3 (x= f, cl, br, i) halide perovskites," *Acta Crystallographica Section B: Structural Science*, vol. 64, no. 6, pp. 702–707, 2008.

[11] P. Tonui, S. O. Oseni, G. Sharma, Q. Yan, and G. T. Mola, "Perovskites photovoltaic solar cells: An overview of current status," *Renewable and Sustainable Energy Reviews*, vol. 91, pp. 1025–1044, 2018.

[12] H. J. Snaith, A. Abate, J. M. Ball, G. E. Eperon, T. Leijtens, N. K. Noel, S. D. Stranks, J. T.-W. Wang, K. Wojciechowski, and W. Zhang, "Anomalous hysteresis in perovskite solar cells," *The journal of physical chemistry letters*, vol. 5, no. 9, pp. 1511–1515, 2014.

[13] X. Yang, W. Wang, R. Ran, W. Zhou, and Z. Shao, "Recent advances in cs2agbibr6-based halide double perovskites as lead-free and inorganic light absorbers for perovskite solar cells," *Energy & Fuels*, vol. 34, no. 9, pp. 10 513–10 528, 2020.

[14] V. Zardetto, B. Williams, A. Perrotta, F. Di Giacomo, M. Verheijen, R. Andriessen, W. Kessels, and M. Creatore, "Atomic layer deposition for perovskite solar cells: Research status, opportunities and challenges," *Sustainable Energy & Fuels*, vol. 1, no. 1, pp. 30–55, 2017.

[15] Z. Hawash, L. K. Ono, and Y. Qi, "Recent advances in spiro-meotad hole transport material and its applications in organic–inorganic halide perovskite solar cells," *Advanced Materials Interfaces*, vol. 5, no. 1, p. 1 700 623, 2018.

[16] S. Ameen, M. A. Rub, S. A. Kosa, K. A. Alamry, M. S. Akhtar, H.-S. Shin, H.-K. Seo, A. M. Asiri, and M. K. Nazeeruddin, "Perovskite solar cells: Influence of hole transporting materials on power conversion efficiency," *ChemSusChem*, vol. 9, no. 1, pp. 10–27, 2016.

[17] J. A. Christians, R. C. Fung, and P. V. Kamat, “An inorganic hole conductor for organo-lead halide perovskite solar cells. improved hole conductivity with copper iodide,” *Journal of the American Chemical Society*, vol. 136, no. 2, pp. 758–764, 2014.

[18] H. Liu, Z. Huang, S. Wei, L. Zheng, L. Xiao, and Q. Gong, “Nano-structured electron transporting materials for perovskite solar cells,” *Nanoscale*, vol. 8, no. 12, pp. 6209–6221, 2016.

[19] Z. Yin, J. Wei, and Q. Zheng, “Interfacial materials for organic solar cells: Recent advances and perspectives,” *Advanced Science*, vol. 3, no. 8, p. 1 500 362, 2016.

[20] S. M. Jassim, N. A. Bakr, and F. I. Mustafa, “Synthesis and characterization of mapbi 3 thin film and its application in c-si/perovskite tandem solar cell,” *Journal of Materials Science: Materials in Electronics*, vol. 31, no. 19, pp. 16 199–16 207, 2020.

[21] S. D. Stranks, G. E. Eperon, G. Grancini, C. Menelaou, M. J. Alcocer, T. Leijtens, L. M. Herz, A. Petrozza, and H. J. Snaith, “Electron-hole diffusion lengths exceeding 1 micrometer in an organometal trihalide perovskite absorber,” *Science*, vol. 342, no. 6156, pp. 341–344, 2013.

[22] T. Oku, “Crystal structures of ch3nh3pbi3 and related perovskite compounds used for solar cells,” *Solar Cells-New Approaches and Reviews*, vol. 1, 2015.

[23] H.-S. Kim, C.-R. Lee, J.-H. Im, K.-B. Lee, T. Moehl, A. Marchioro, S.-J. Moon, R. Humphry-Baker, J.-H. Yum, J. E. Moser, *et al.*, “Lead iodide perovskite sensitized all-solid-state submicron thin film mesoscopic solar cell with efficiency exceeding 9%,” *Scientific reports*, vol. 2, no. 1, pp. 1–7, 2012.

[24] S. Bhattarai, A. Sharma, and T. Das, “Performance enhancement for scattering effect in perovskite solar cell with distinct cathode materials,” in *Electronic Systems and Intelligent Computing*, Springer, 2020, pp. 965–971.

[25] Z. Yang, B. H. Babu, S. Wu, T. Liu, S. Fang, Z. Xiong, L. Han, and W. Chen, “Review on practical interface engineering of perovskite solar cells: From efficiency to stability,” *Solar Rrl*, vol. 4, no. 2, p. 1 900 257, 2020.

[26] M. Ye, C. He, J. Iocozzia, X. Liu, X. Cui, X. Meng, M. Rager, X. Hong, X. Liu, and Z. Lin, “Recent advances in interfacial engineering of perovskite solar cells,” *Journal of Physics D: Applied Physics*, vol. 50, no. 37, p. 373 002, 2017.

[27] P. Schulz, D. Cahen, and A. Kahn, “Halide perovskites: Is it all about the interfaces?” *Chemical reviews*, vol. 119, no. 5, pp. 3349–3417, 2019.

[28] S. Shao and M. A. Loi, “The role of the interfaces in perovskite solar cells,” *Advanced Materials Interfaces*, vol. 7, no. 1, p. 1 901 469, 2020.

[29] H. Jin, E. Debroye, M. Keshavarz, I. G. Scheblykin, M. B. Roeffaers, J. Hofkens, and J. A. Steele, “It’s a trap! on the nature of localised states and charge trapping in lead halide perovskites,” *Materials Horizons*, vol. 7, no. 2, pp. 397–410, 2020.

[30] J. Peng, J. I. Khan, W. Liu, E. Ugur, T. Duong, Y. Wu, H. Shen, K. Wang, H. Dang, E. Aydin, *et al.*, “A universal double-side passivation for high open-circuit voltage in perovskite solar cells: Role of carbonyl groups in poly (methyl methacrylate),” *Advanced Energy Materials*, vol. 8, no. 30, p. 1 801 208, 2018.

[31] Q. Jiang, Y. Zhao, X. Zhang, X. Yang, Y. Chen, Z. Chu, Q. Ye, X. Li, Z. Yin, and J. You, “Surface passivation of perovskite film for efficient solar cells,” *Nature Photonics*, vol. 13, no. 7, pp. 460–466, 2019.

[32] B. Li, Y. Zhang, L. Fu, T. Yu, S. Zhou, L. Zhang, and L. Yin, “Surface passivation engineering strategy to fully-inorganic cubic cspbi 3 perovskites for high-performance solar cells,” *Nature communications*, vol. 9, no. 1, pp. 1–8, 2018.

[33] B. Chaudhary, A. Kulkarni, A. K. Jena, M. Ikegami, Y. Udagawa, H. Kunugita, K. Ema, and T. Miyasaka, “Poly (4-vinylpyridine)-based interfacial passivation to enhance voltage and moisture stability of lead halide perovskite solar cells,” *ChemSusChem*, vol. 10, no. 11, pp. 2473–2479, 2017.

[34] C. M. Wolff, F. Zu, A. Paulke, L. P. Toro, N. Koch, and D. Neher, “Reduced interface-mediated recombination for high open-circuit voltages in ch3nh3pbi3 solar cells,” *Advanced materials*, vol. 29, no. 28, p. 1 700 159, 2017.

[35] M. Li, X. Yan, Z. Kang, Y. Huan, Y. Li, R. Zhang, and Y. Zhang, “Hydrophobic polystyrene passivation layer for simultaneously improved efficiency and stability in perovskite solar cells,” *ACS applied materials & interfaces*, vol. 10, no. 22, pp. 18 787–18 795, 2018.

[36] X. Wen, J. Wu, M. Ye, D. Gao, and C. Lin, “Interface engineering via an insulating polymer for highly efficient and environmentally stable perovskite solar cells,” *Chemical Communications*, vol. 52, no. 76, pp. 11 355–11 358, 2016.

[37] Y. Bai, H. Yu, Z. Zhu, K. Jiang, T. Zhang, N. Zhao, S. Yang, and H. Yan, “High performance inverted structure perovskite solar cells based on a pcbm: Polystyrene blend electron transport layer,” *Journal of Materials Chemistry A*, vol. 3, no. 17, pp. 9098–9102, 2015.

[38] B. Krogmeier, F. Staub, D. Grabowski, U. Rau, and T. Kirchartz, “Quantitative analysis of the transient photoluminescence of ch 3 nh 3 pbi 3/pc 61 bm heterojunctions by numerical simulations,” *Sustainable Energy & Fuels*, vol. 2, no. 5, pp. 1027–1034, 2018.

[39] C. S. Ponseca Jr, E. M. Hutter, P. Piatkowski, B. Cohen, T. Pascher, A. Douhal, A. Yartsev, V. Sundström, and T. J. Savenije, “Mechanism of charge transfer and recombination dynamics in organo metal halide perovskites and organic electrodes, pcbm, and spiro-ometad: Role of dark carriers,” *Journal of the American Chemical Society*, vol. 137, no. 51, pp. 16 043–16 048, 2015.

[40] V. M. Caselli, Z. Wei, M. M. Ackermans, E. M. Hutter, B. Ehrler, and T. J. Savenije, “Charge carrier dynamics upon sub-bandgap excitation in methylammonium lead iodide thin films: Effects of urbach tail, deep defects, and two-photon absorption,” *ACS Energy Letters*, vol. 5, no. 12, pp. 3821–3827, 2020.

[41] D. A. Neamen, *Semiconductor physics and devices: basic principles*. New York, NY: McGraw-Hill, 2012.

[42] D. Guo, V. M. Caselli, E. M. Hutter, and T. J. Savenije, “Comparing the calculated fermi level splitting with the open-circuit voltage in various perovskite cells,” *ACS Energy Letters*, vol. 4, no. 4, pp. 855–860, 2019.

[43] T. Hellmann, C. Das, T. Abzieher, J. A. Schwenzer, M. Wussler, R. Dachauer, U. W. Paetzold, W. Jaegermann, and T. Mayer, “The electronic structure of mapi-based perovskite solar cells: Detailed band diagram determination by photoemission spectroscopy comparing classical and inverted device stacks,” *Advanced Energy Materials*, vol. 10, no. 42, p. 2 002 129, 2020.

[44] J. Byeon, J. Kim, J.-Y. Kim, G. Lee, K. Bang, N. Ahn, and M. Choi, “Charge transport layer-dependent electronic band bending in perovskite solar cells and its correlation to light-induced device degradation,” *ACS Energy Letters*, vol. 5, no. 8, pp. 2580–2589, 2020.

[45] D. Amasev, E. Krivogina, O. Khalipova, A. Zabolotskaya, V. Kozik, I. Ivonin, S. Kozyukhin, and A. Kazanskii, “The effect of the air environment and prolonged illumination on conductivity and photoconductivity of organic-inorganic perovskite ch3nh3pbi3 films,” in *Journal of Physics: Conference Series*, IOP Publishing, vol. 1611, 2020, p. 012 043.

[46] W.-A. Quitsch, D. W. deQuilettes, O. Pfingsten, A. Schmitz, S. Ognjanovic, S. Jariwala, S. Koch, M. Winterer, D. S. Ginger, and G. Bacher, “The role of excitation energy in photobrightening and photodegradation of halide perovskite thin films,” *The journal of physical chemistry letters*, vol. 9, no. 8, pp. 2062–2069, 2018.

[47] A. F. Akbulatov, L. A. Frolova, N. N. Dremova, I. Zhidkov, V. M. Martynenko, S. A. Tsarev, S. Y. Luchkin, E. Z. Kurmaev, S. M. Aldoshin, K. J. Stevenson, *et al.*, “Light or heat: What is killing lead halide perovskites under solar cell operation conditions?” *The journal of physical chemistry letters*, vol. 11, no. 1, pp. 333–339, 2019.

[48] E. M. Tennyson, J. M. Howard, B. Roose, J. L. Garrett, J. N. Munday, A. Abate, and M. S. Leite, “The effects of incident photon energy on the time-dependent voltage response of lead halide perovskites,” *Chemistry of Materials*, vol. 31, no. 21, pp. 8969–8976, 2019.

[49] X. Deng, X. Wen, J. Zheng, T. Young, C. F. J. Lau, J. Kim, M. Green, S. Huang, and A. Ho-Baillie, “Dynamic study of the light soaking effect on perovskite solar cells by in-situ photoluminescence microscopy,” *Nano Energy*, vol. 46, pp. 356–364, 2018.

[50] G. Tumen-Ulzii, C. Qin, T. Matsushima, M. R. Leyden, U. Balijipalli, D. Klotz, and C. Adachi, “Understanding the degradation of spiro-ometad-based perovskite solar cells at high temperature,” *Solar RRL*, vol. 4, no. 10, p. 2 000 305, 2020.

[51] D. W. DeQuilettes, W. Zhang, V. M. Burlakov, D. J. Graham, T. Leijtens, A. Osherov, V. Bulović, H. J. Snaith, D. S. Ginger, and S. D. Stranks, “Photo-induced halide redistribution in organic–inorganic perovskite films,” *Nature communications*, vol. 7, no. 1, pp. 1–9, 2016.

[52] S. Chen, X. Wen, S. Huang, F. Huang, Y.-B. Cheng, M. Green, and A. Ho-Baillie, “Light illumination induced photoluminescence enhancement and quenching in lead halide perovskite,” *Solar Rrl*, vol. 1, no. 1, p. 1 600 001, 2017.

[53] F. Zheng, X. Wen, T. Bu, S. Chen, J. Yang, W. Chen, F. Huang, Y. Cheng, and B. Jia, “Slow response of carrier dynamics in perovskite interface upon illumination,” *ACS applied materials & interfaces*, vol. 10, no. 37, pp. 31 452–31 461, 2018.

[54] T. Savenije, D. Guo, V. Caselli, and E. Hutter, “Quantifying charge-carrier mobilities and recombination rates in metal halide perovskites from time-resolved microwave photoconductivity measurements,” English, *Advanced Energy Materials*, vol. 10, no. 26, 2020, ISSN: 1614-6832. DOI: 10.1002/aenm.201903788.

[55] E. M. Hutter, J.-J. Hofman, M. L. Petrus, M. Moes, R. D. Abellón, P. Docampo, and T. J. Savenije, “Charge transfer from methylammonium lead iodide perovskite to organic transport materials: Efficiencies, transfer rates, and interfacial recombination,” *Advanced Energy Materials*, vol. 7, no. 13, p. 1 602 349, 2017.

[56] A. Kojima, K. Teshima, Y. Shirai, and T. Miyasaka, “Organometal halide perovskites as visible-light sensitizers for photovoltaic cells,” *Journal of the American Chemical Society*, vol. 131, no. 17, pp. 6050–6051, 2009.

[57] D. W. deQuilettes, K. Frohna, D. Emin, T. Kirchartz, V. Bulovic, D. S. Ginger, and S. D. Stranks, “Charge-carrier recombination in halide perovskites: Focus review,” *Chemical reviews*, vol. 119, no. 20, pp. 11 007–11 019, 2019.

[58] T. W. Crothers, R. L. Milot, J. B. Patel, E. S. Parrott, J. Schlipf, P. Müller-Buschbaum, M. B. Johnston, and L. M. Herz, “Photon reabsorption masks intrinsic bimolecular charge-carrier recombination in ch3nh3pbi3 perovskite,” *Nano letters*, vol. 17, no. 9, pp. 5782–5789, 2017.

[59] Y. Yamada, T. Yamada, and Y. Kanemitsu, “Free carrier radiative recombination and photon recycling in lead halide perovskite solar cell materials,” *Bulletin of the Chemical Society of Japan*, vol. 90, no. 10, pp. 1129–1140, 2017.

A

Appendix

A.1. Structural and Optical Properties

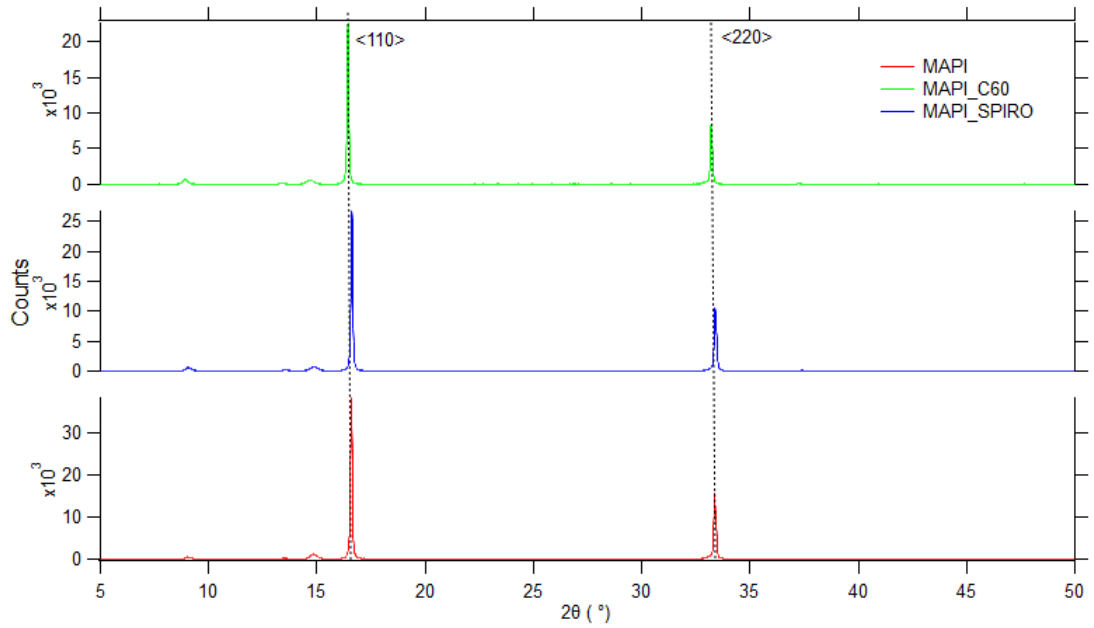

Figure A.1: XRD of pristine MAPI and with C_{60} and Spiro-MeOTAD

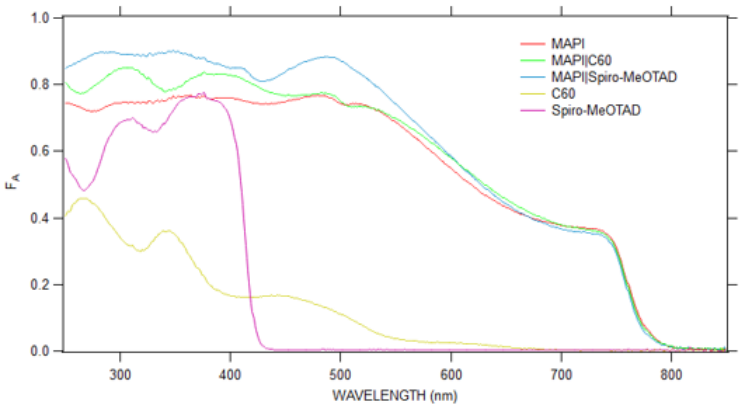

Figure A.2: Absorption of pristine MAPI and with C_{60} and Spiro-MeOTAD and the pristine transport layers from the front

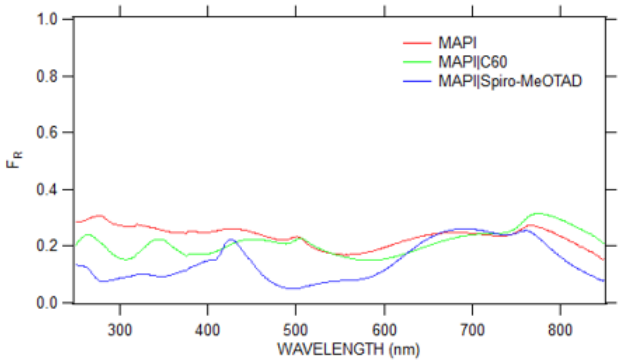

Figure A.3: Reflection of pristine MAPI and with C_{60} and Spiro-MeOTAD from the front

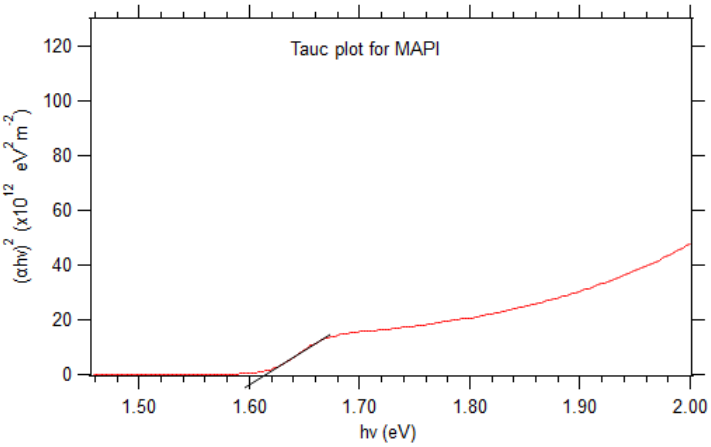

Figure A.4: Tauc plot for MAPI for calculation of band gap

A.2. Bias Light Experiment

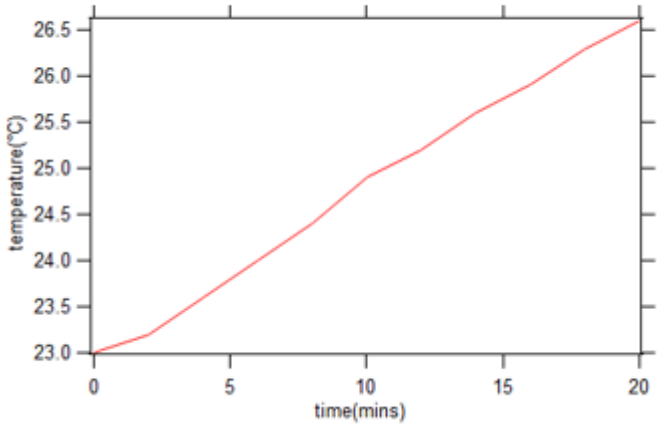

Figure A.5: Temperature increase of the pristine MAPI under continuous illumination in the experimental timeframe

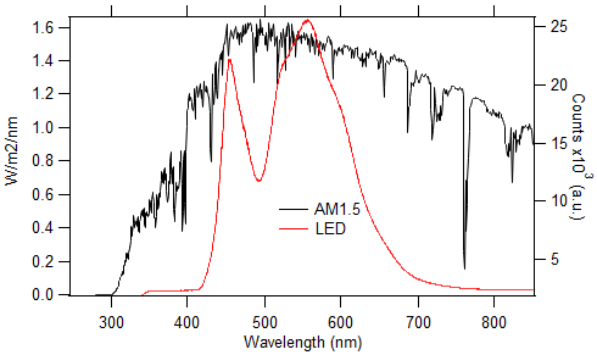

(a) Power Spectrum of white LED vs AM1.5

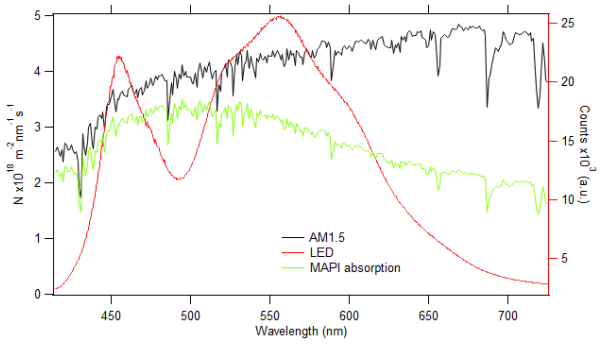

(b) Photon intensity emitted and absorbed per wavelength per time

The white LED has an emission in the wavelength range of 415-725nm. The number of photons absorbed by the MAPI under 1 sun (AM 1.5) is found out by correcting the number of photons emitted under 1 sun by the fraction absorption of the MAPI. It was found out to be $8.237*10^{16}$photons/(cm^2s).The power of 1sun in this wavelength range is 44.28mW/cm^2. The full power of the LED was 100mW/cm2 as measured by the pyranometer.
The intensity of the LED in the two setups measured by the silicon photodetector used in the experiment were found to be 9.568mW/cm^2 and 1.316mW/cm^2. The number of photons emitted at the higher power can be approximately calculated by ($8.237*10^{16}$photons/(cm^2s) *9.568)/44.28 and was found to be $1.78*10^{16}$ photons/ (cm^2s).

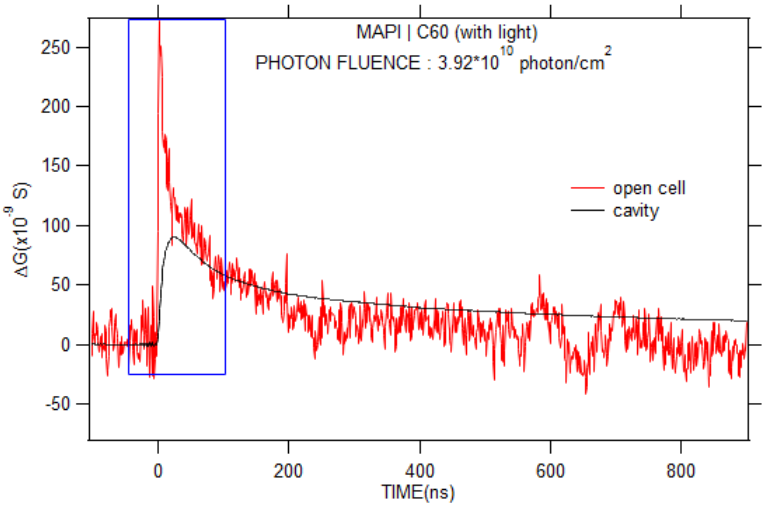

Figure A.7: Example of effect of time resolution in open cell vs cavity

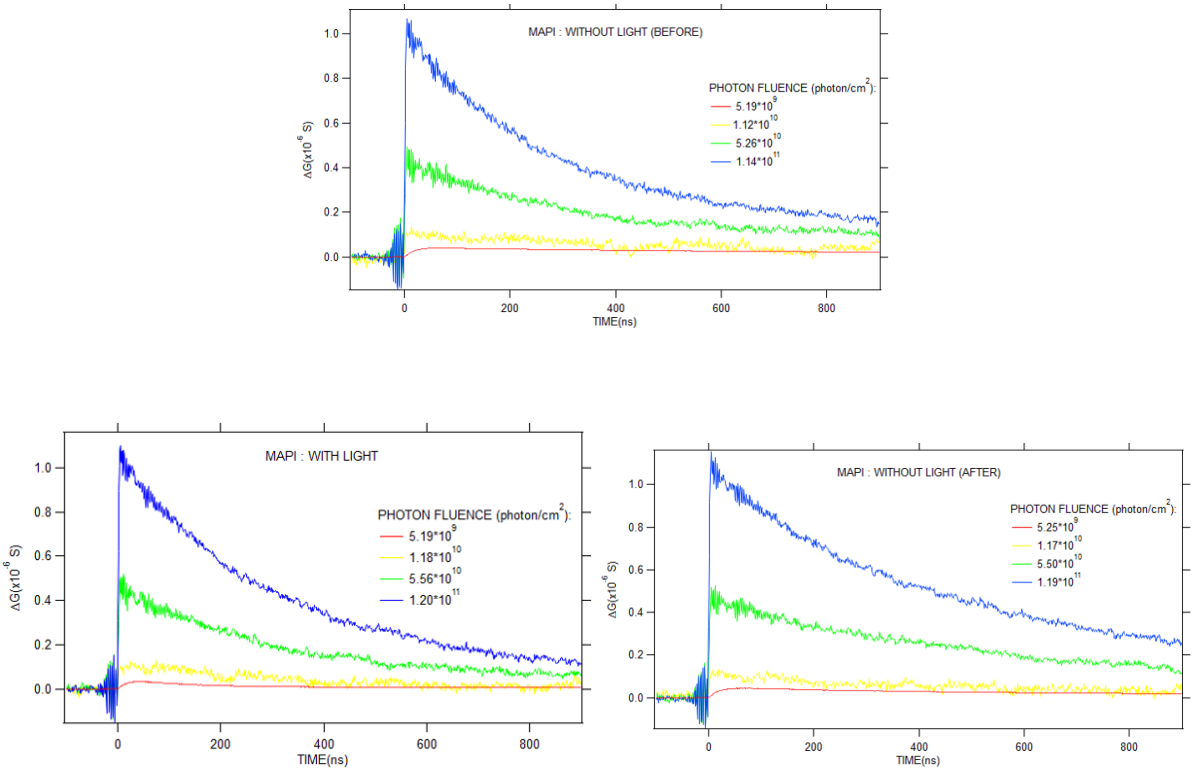

Figure A.8: Backside measurement of TRMC of MAPI

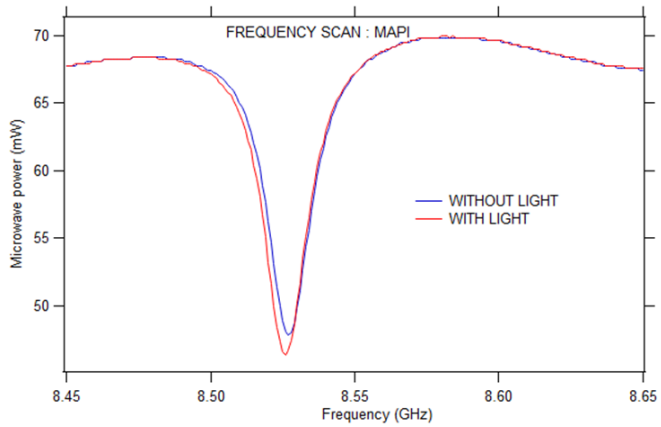

Figure A.9: Frequency scan of MAPI during frontside illumination at high bias intensity

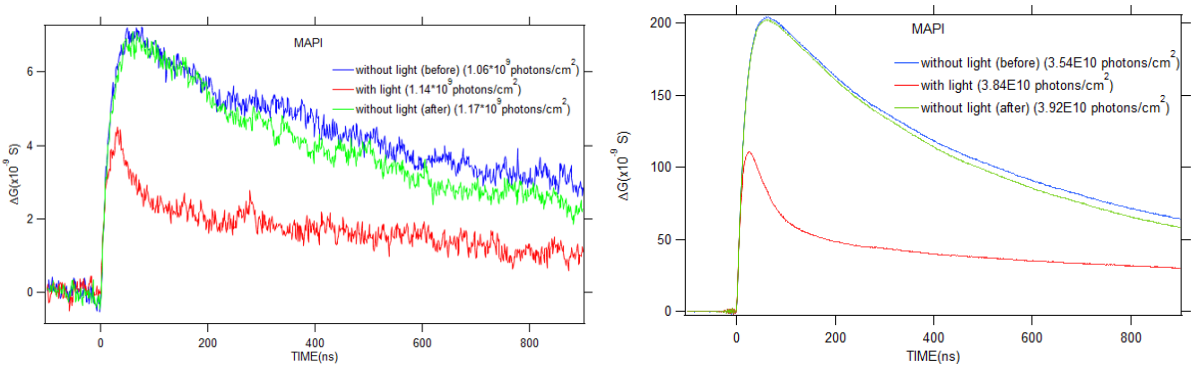

(a) Low photon fluence of laser

(b) High photon fluence of laser

Figure A.10: Comparison of TRMC traces of MAPI with light and without light before and after illumination with white light from frontside

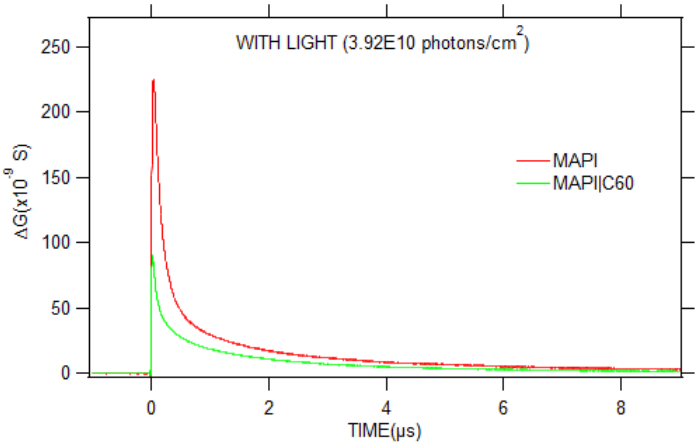

Figure A.11: TRMC trace of MAPI|C_{60} with continuous illumination under high bias power of 96.68W/m^2 in longer time scale

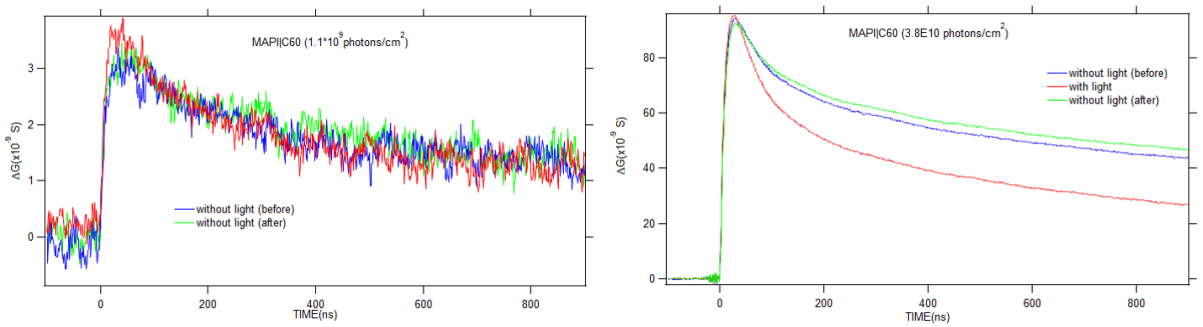

(a) Low photon fluence of laser

(b) High photon fluence of laser

Figure A.12: Comparison of TRMC traces of MAPI |C_{60} with light and without light before and after illumination with white light from frontside

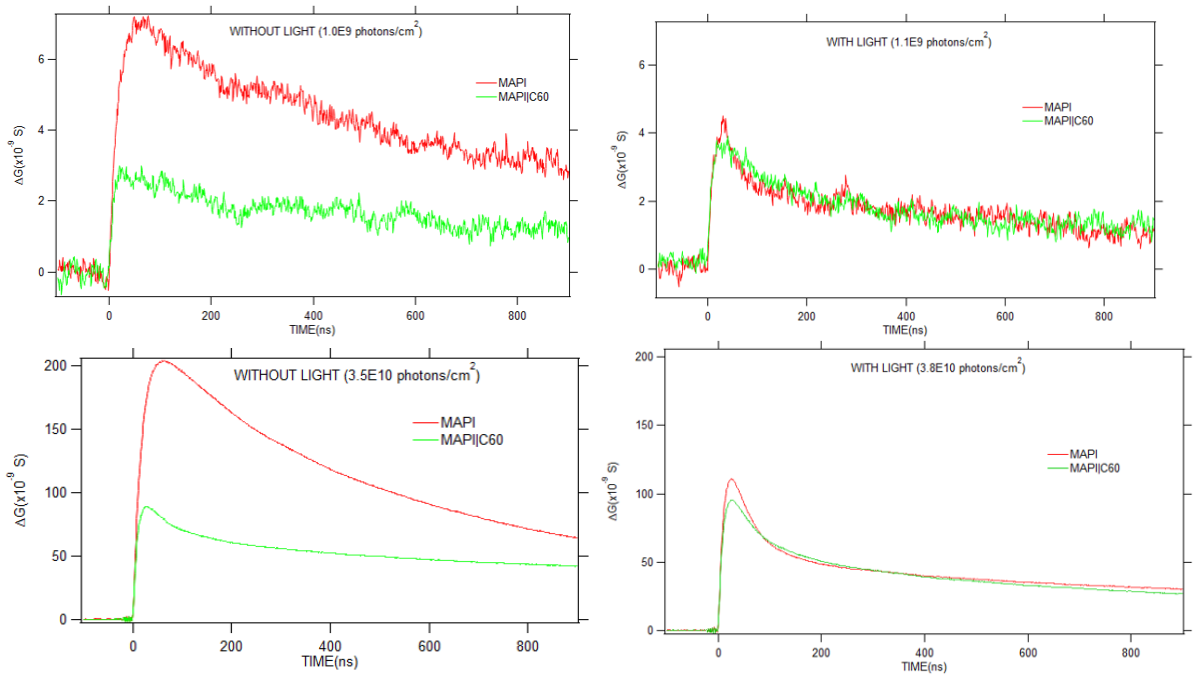

Figure A.13: Saturation of the C_{60} layer during frontside measurement

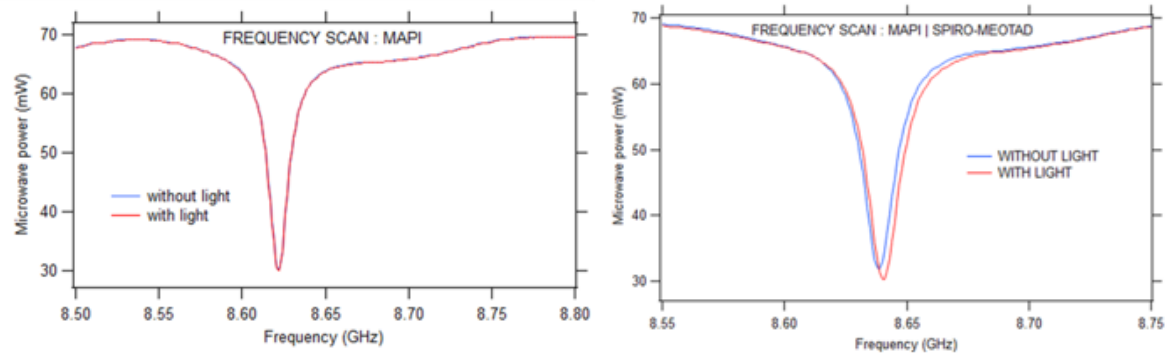

Figure A.14: Frequency scan measured at low bias power at room temperature from frontside

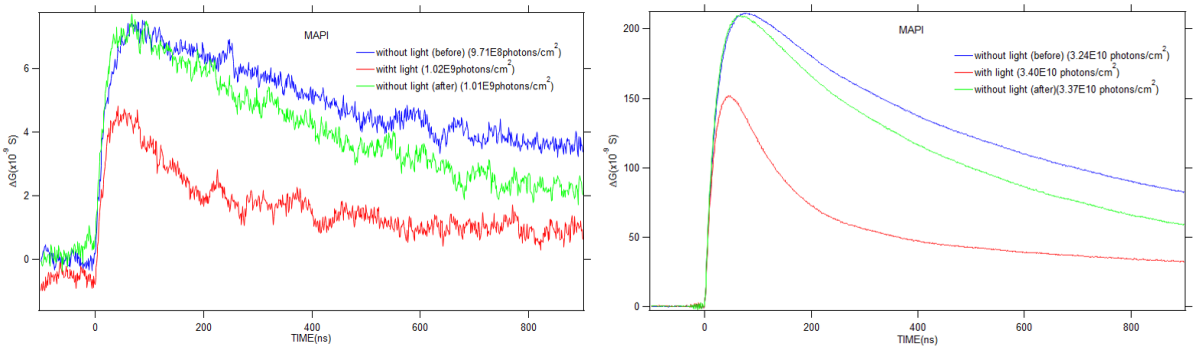

(a) Low photon fluence of laser

(b) High photon fluence of laser

Figure A.15: Comparison of TRMC traces of MAPI with light and without light before and after illumination with white light from frontside at low bias intensity at room temperature

A.3. Modelling of TRMC traces

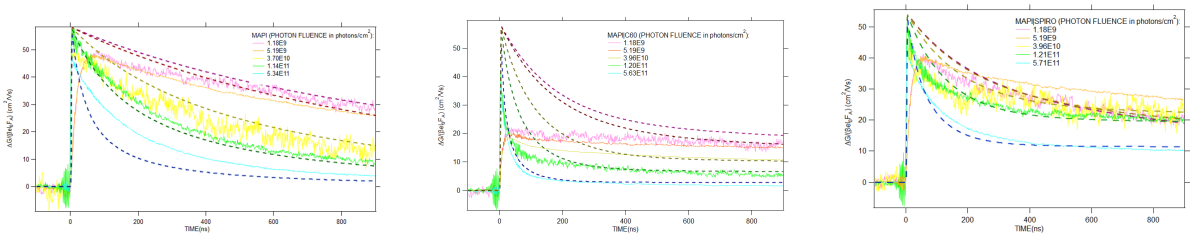

Figure A.16: Modelling of TRMC traces in dark (before continuous illumination)

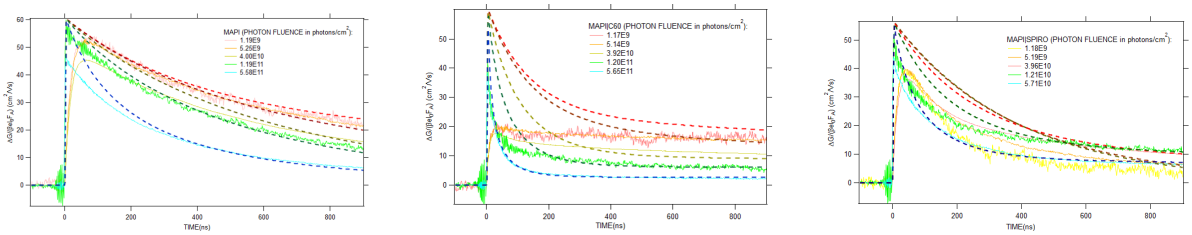

Figure A.17: Modelling of TRMC traces in dark (after the continuous illumination)